










A positivity-preserving adaptive-order finite-difference scheme for GRMHD

Nils Deppe^{1,2,3} , Lawrence E. Kidder² , Saul A. Teukolsky^{2,3} , Marceline S. Bonilla⁴ , François Hébert³ , Yoonsoo Kim³ , Mark A. Scheel³ , William Throwe² , and Nils L. Vu³ 

¹Department of Physics, Cornell University, Ithaca, NY, 14853, USA

²Cornell Center for Astrophysics and Planetary Science, Cornell University, Ithaca, New York 14853, USA

³Theoretical Astrophysics 350-17, California Institute of Technology, Pasadena, CA 91125, USA

⁴Nicholas and Lee Begovich Center for Gravitational-Wave Physics and Astronomy, California State University Fullerton, Fullerton, CA 92834, USA

E-mail: nd357@cornell.edu

Abstract. We present an adaptive-order positivity-preserving conservative finite-difference scheme that allows a high-order solution away from shocks and discontinuities while guaranteeing positivity and robustness at discontinuities. This is achieved by monitoring the relative power in the highest mode of the reconstructed polynomial and reducing the order when the polynomial series no longer converges. Our approach is similar to the multidimensional optimal order detection (MOOD) strategy, but differs in several ways. The approach is *a priori* and so does not require retaking a time step. It can also readily be combined with positivity-preserving flux limiters that have gained significant traction in computational astrophysics and numerical relativity. This combination ultimately guarantees a physical solution both during reconstruction and time stepping. We demonstrate the capabilities of the method using a standard suite of very challenging 1d, 2d, and 3d general relativistic magnetohydrodynamics test problems.

Keywords: Hyperbolic PDE, adaptive order, MOOD, Finite Volumes, Finite Difference, WENO, WCNS, Higher order Godunov schemes, Positivity, Hydrodynamics

1. Introduction

Godunov's theorem[1] tells us that in the numerical solution of conservation laws, high-order linear schemes cannot prevent oscillations from appearing, be they physical or unphysical. Nonlinear hybridization has been used to circumvent Godunov's theorem by reconstructing a high-order polynomial using nonlinear combinations of the variables. All modern methods such as essentially non-oscillatory (ENO)[2, 3, 4, 5, 6], weighted ENO (WENO)[7, 8], and weighted compact nonlinear schemes (WCNS)[9, 10, 11] use nonlinear hybridization to achieve higher-than-first-order accuracy. WENO and WCNS schemes are commonly used to construct high-order finite-difference (FD) schemes. One major challenge in using high-order FD schemes with complicated equations is maintaining physical realizability of the solution, such as positivity of the density and pressure. We develop a new adaptive order WENO-type method that guarantees physical realizability during the reconstruction by reconstructing the primitive variables as opposed to the conserved or characteristic variables. We expect such methods to be particularly effective for binary neutron star merger simulations, both magnetized and unmagnetized, where achieving high-order convergence is attracting increasingly more efforts [12, 13, 14, 15, 16].

Existing WENO and WCNS schemes work by combining several low-order stencils into a high-order stencil that interpolates the solution within a FD cell. How much each low-order stencil contributes to the final result is determined by use of an oscillation or smoothness indicator. The more oscillatory a stencil is, the less it contributes to the overall reconstruction polynomial. FD schemes fall into two broad categories: flux vector splitting (FVS) and flux difference splitting (FDS). FVS schemes write the numerical flux as a linear combination of a right- and left-moving part, then reconstruct the numerical fluxes to the cell boundaries. FDS schemes reconstruct the conserved, primitive, or characteristic variables to the cell boundaries, and then use a numerical flux at the cell boundary. The advantage of FDS over FVS is that more numerical fluxes can be used with them since the numerical flux need not be split (see, e.g. [17] for a helpful review).

Reconstructing the characteristic variables yields very good results with FDS schemes (e.g. [18]). However, for increasingly complex physical systems computing the characteristic variables becomes analytically intractable and needs to be done numerically. Unfortunately, computing the characteristic variables numerically is often very expensive for these systems and so does not present a realistic alternative. An important example in practice is the equations of general relativistic magnetohydrodynamics (GRMHD).

Another issue that arises when reconstructing the conserved or characteristic variables is that the reconstructed solution may not be physically realizable. For example, the density of the reconstructed state may be negative (see, e.g. [19, 20, 21]). Reconstructing the primitive variables permits straightforward guarding against such unphysical reconstructed states. Flux limiters have been used to maintain a physically realizable solution [22] when using FVS schemes, even in numerical relativity [13]. However, when a characteristic decomposition is not available, the dissipative Rusanov or local Lax-Friedrichs numerical flux needs to be used in the FVS scheme. Another strategy for maintaining positivity when reconstructing the conserved variables is the flattener algorithm [23], which was originally proposed for finite-volume methods. The flattener smoothly interpolates between a first-order and high-order reconstruction in a way that the reconstructed polynomial is physically realizable. The main disadvantage of the flattener compared to the new method presented here is that the flattener does not provide a way of determining what order FD derivative should be used.

Adaptive-order WENO schemes have recently been presented that combine one or more high-order stencils with robust low-order stencils [24, 25, 26, 27, 28]. The high-order stencil is used if it is not too oscillatory, while the low-order standard WENO stencils are used if the high-order stencil is inadmissible. A similar approach called multidimensional optimal-order detection (MOOD) [29, 30, 31] has also been presented where unlimited reconstruction is generally used, but the order is decreased *a posteriori* and discretely. That is, after a time step is taken, the result is accepted only if the solution passes numerical and physical admissibility conditions; otherwise the time step is redone using a lower order scheme.

We address the difficulty of achieving high-order accuracy while maintaining physical realizability and robustness by:

- introducing a new oscillation indicator that directly measures the amount of power in the high-order polynomials of the reconstruction,
- weighting the reconstructed stencils by physical realizability instead of just numerical admissibility,
- adapting the order of the FD derivative according to the order of the reconstruction to avoid differentiating across discontinuities,
- providing two general implementations, one using weighting of the different stencils and one discretely selecting the highest order admissible stencil.

We present the new oscillation indicator in §2.2, describe how to include physical realizability into the scheme in §2.3, and discuss the FD derivative adaptation in §2.4. In §2.6 we discuss how to make the discrete stencil selection process described in §2.2 continuous by combining the new oscillation indicator with physical realizability conditions and using a sigmoid-like function for blending the stencils. This method of including the physical realizability conditions into the stencil weights can readily be incorporated into other WENO and WCNS schemes. Finally, in §3 we show results from a large variety of standard and difficult test problems in 1d, 2d, and 3d GRMHD. In Appendix A we briefly comment on how the scheme presented here can be used in a discontinuous Galerkin-finite difference hybrid method as described in [32].

2. Method

We first present the new *a priori* adaptive order scheme in 1d, including a description of the positivity-preserving strategy. We then use the equations of ideal general relativistic magnetohydrodynamics (GRMHD) as a concrete example.

We are interested in solving general conservation laws of the form

$$\partial_t u + \partial_i F^i(u) = S(u), \tag{1}$$

where u is the vector of conserved variables, Latin indices later in the alphabet (such as i) denote spatial indices, F^i is the flux vector, and S is the source vector. Here and throughout we implicitly sum over repeated indices. We denote the primitive variables as p . Since we are ultimately interested in systems where the characteristic variables are either not known or are very expensive to compute, we seek to develop a robust, positivity-preserving non-oscillatory scheme where the primitive variables are reconstructed to cell interfaces.

Conservative finite-difference schemes evolve the cell-center values, but require the cell-face values (the midpoints along each axis) for solving the Riemann problem and for computing the finite-difference derivatives of the flux. That is, the semi-discrete form of Eq. 1 is

$$\partial_t u_i + \frac{G_{i+1/2}^i - G_{i-1/2}^i}{\Delta x^i} = S_i, \tag{2}$$

where hatted indices denote grid points/cells, and G^i is the numerical flux given by (approximately) solving the Riemann problem at the cell interface. The FD derivative in Eq. 2 is of second order, but we show how this can be extended to higher order in §2.4.

In §2.4 we also describe our new method of adjusting the order of the finite-difference derivative based on the local smoothness of the solution.

WENO and WCNS schemes use nonlinear reconstruction and are very robust when applied to the characteristic variables. When applied to the primitive variables they can lead to staircasing, where small-scale oscillations are present in smooth regions [33]. We opt for a different approach to obtain a high-order non-oscillatory scheme that somewhat resembles multidimensional optimal-order detection (MOOD)[29, 30, 31]. We combine several new ingredients: first, we present a new method of obtaining a high-order polynomial based on spectral elements; second we present a new *a priori* detection algorithm for determining whether or not the reconstructed stencil is acceptable; third we present a method to combine our adaptive-order scheme with a positivity-preserving strategy; and finally we present a method of adjusting the FD order to increase stability without the accuracy of the scheme deteriorating in smooth regions. We will refer to the method we present as a positivity-preserving adaptive-order (PPAO‡) scheme where we postfix with hyphens the orders used. For example, we denote a PPAO scheme with the order decrementing from fifth to third to first as PPAO5-3-1. In §2.1 we carry out a detailed derivation of the fifth-order scheme. We then provide a table of the coefficients for seventh- and ninth-order schemes.

2.1. High-order reconstruction

We construct a fifth-order scheme using a polynomial of degree four from the solution $\{p_{\hat{j}-2}, p_{\hat{j}-1}, p_{\hat{j}}, p_{\hat{j}+1}, p_{\hat{j}+2}\}$, where \hat{j} indexes the cell. We do this by setting up a spectral element on the interval $[x_{\hat{j}-5/2}, x_{\hat{j}+5/2}]$ with Legendre basis functions. The interval is remapped to the logical coordinate $\xi \in [-1, 1]$ where the Legendre basis functions are defined. It is important to note that this differs from the more common approach of remapping the interval $[x_{\hat{j}-1/2}, x_{\hat{j}+1/2}]$ to $\xi \in [-1, 1]$. Defining the basis functions over the larger interval is key to detecting oscillations over the region the polynomials are fit. This is one crucial way our method differs from previous literature and is what makes it very robust at detecting non-smooth solutions. We denote the n^{th} degree Legendre polynomials by $P_n(\xi)$. Within the spectral element we expand the solution as

$$p_j(\xi) = \sum_{n=0}^N c_{j,n} P_n(\xi), \tag{3}$$

‡ Pronounced “pow”.

Table 1. Coefficients for reconstructing the polynomials at the cell-face values at different orders.

Degree	Face	$\hat{j} - 4$	$\hat{j} - 3$	$\hat{j} - 2$	$\hat{j} - 1$	\hat{j}	$\hat{j} + 1$	$\hat{j} + 2$	$\hat{j} + 3$	$\hat{j} + 4$
2	$\hat{j} - 1/2$				$\frac{3}{8}$	$\frac{3}{4}$	$-\frac{1}{8}$			
	$\hat{j} + 1/2$				$-\frac{1}{8}$	$\frac{3}{4}$	$\frac{3}{8}$			
4	$\hat{j} - 1/2$			$-\frac{5}{128}$	$\frac{15}{32}$	$\frac{45}{64}$	$-\frac{5}{32}$	$\frac{3}{128}$		
	$\hat{j} + 1/2$			$\frac{3}{128}$	$-\frac{5}{32}$	$\frac{45}{64}$	$\frac{15}{32}$	$-\frac{5}{128}$		
6	$\hat{j} - 1/2$		$\frac{7}{1024}$	$-\frac{35}{512}$	$\frac{525}{1024}$	$\frac{175}{256}$	$-\frac{175}{1024}$	$\frac{21}{512}$	$-\frac{5}{1024}$	
	$\hat{j} + 1/2$		$-\frac{5}{1024}$	$\frac{21}{512}$	$-\frac{175}{1024}$	$\frac{175}{256}$	$\frac{525}{1024}$	$-\frac{35}{512}$	$\frac{7}{1024}$	
8	$\hat{j} - 1/2$	$-\frac{45}{32768}$	$\frac{63}{4096}$	$-\frac{735}{8192}$	$\frac{2205}{4096}$	$\frac{11025}{16384}$	$-\frac{735}{4096}$	$\frac{441}{8192}$	$-\frac{45}{4096}$	$\frac{35}{32768}$
	$\hat{j} + 1/2$	$\frac{35}{32768}$	$-\frac{45}{4096}$	$\frac{441}{8192}$	$-\frac{735}{4096}$	$\frac{11025}{16384}$	$\frac{2205}{4096}$	$-\frac{735}{8192}$	$\frac{63}{4096}$	$-\frac{45}{32768}$

where $c_{j,n}$ are the modal coefficients for the expansion about the \hat{j}^{th} cell. The coefficients $c_{j,n}$ are computed by solving the linear system

$$\begin{pmatrix} P_0(\xi_{\hat{j}-2}) & P_1(\xi_{\hat{j}-2}) & P_2(\xi_{\hat{j}-2}) & P_3(\xi_{\hat{j}-2}) & P_4(\xi_{\hat{j}-2}) \\ P_0(\xi_{\hat{j}-1}) & P_1(\xi_{\hat{j}-1}) & P_2(\xi_{\hat{j}-1}) & P_3(\xi_{\hat{j}-1}) & P_4(\xi_{\hat{j}-1}) \\ P_0(\xi_{\hat{j}}) & P_1(\xi_{\hat{j}}) & P_2(\xi_{\hat{j}}) & P_3(\xi_{\hat{j}}) & P_4(\xi_{\hat{j}}) \\ P_0(\xi_{\hat{j}+1}) & P_1(\xi_{\hat{j}+1}) & P_2(\xi_{\hat{j}+1}) & P_3(\xi_{\hat{j}+1}) & P_4(\xi_{\hat{j}+1}) \\ P_0(\xi_{\hat{j}+2}) & P_1(\xi_{\hat{j}+2}) & P_2(\xi_{\hat{j}+2}) & P_3(\xi_{\hat{j}+2}) & P_4(\xi_{\hat{j}+2}) \end{pmatrix} \begin{pmatrix} c_0 \\ c_1 \\ c_2 \\ c_3 \\ c_4 \end{pmatrix} = \begin{pmatrix} p_{\hat{j}-2} \\ p_{\hat{j}-1} \\ p_{\hat{j}} \\ p_{\hat{j}+1} \\ p_{\hat{j}+2} \end{pmatrix}, \quad (4)$$

where we have used the notation $\xi(x_j)$ to represent the function that maps the x coordinates into the ξ coordinates. Assuming uniform spacing in ξ we find that

$$\begin{pmatrix} c_0 \\ c_1 \\ c_2 \\ c_3 \\ c_4 \end{pmatrix} = \begin{pmatrix} 275/1152 & 25/288 & 67/192 & 25/288 & 275/1152 \\ -55/96 & -5/48 & 0 & 5/48 & 55/96 \\ 1525/2016 & -475/504 & 125/336 & -475/504 & 1525/2016 \\ -25/48 & 25/24 & 0 & -25/24 & 25/48 \\ 125/336 & -125/84 & 125/56 & -125/84 & 125/336 \end{pmatrix} \begin{pmatrix} p_{\hat{j}-2} \\ p_{\hat{j}-1} \\ p_{\hat{j}} \\ p_{\hat{j}+1} \\ p_{\hat{j}+2} \end{pmatrix}. \quad (5)$$

In practice we never need to perform the matrix multiplication in Eq. (5) since we can precompute the values $p_{\hat{j}-1/2}$ and $p_{\hat{j}+1/2}$ analytically in terms of $\{p_{\hat{j}-2}, p_{\hat{j}-1}, p_{\hat{j}}, p_{\hat{j}+1}, p_{\hat{j}+2}\}$.

The reconstructed face values are

$$\begin{aligned} p_{\hat{j}-1/2} &= -\frac{5}{128}p_{\hat{j}-2} + \frac{15}{32}p_{\hat{j}-1} + \frac{45}{64}p_{\hat{j}} - \frac{5}{32}p_{\hat{j}+1} + \frac{3}{128}p_{\hat{j}+2}, \\ p_{\hat{j}+1/2} &= \frac{3}{128}p_{\hat{j}-2} - \frac{5}{32}p_{\hat{j}-1} + \frac{45}{64}p_{\hat{j}} + \frac{15}{32}p_{\hat{j}+1} - \frac{5}{128}p_{\hat{j}+2}. \end{aligned} \quad (6)$$

Here $p_{\hat{j}-1/2}$ is the *right* state of the $\hat{j} - 1/2$ interface and $p_{\hat{j}+1/2}$ is the *left* state of the $\hat{j} + 1/2$ interface. By using the same stencil but shifted by one cell to the left or right, the left state on $\hat{j} - 1/2$ and the right state on $\hat{j} + 1/2$ are computed. We show coefficients for evaluating polynomials of degree 2, 4, 6, and 8 at the cell interfaces in table 1.

2.2. Oscillation detection

With a polynomial for reconstructing the face values in hand, we need to determine how oscillatory the polynomial is and whether or not to use it. For a spectral expansion such as the one given in Eq. 3, higher-degree basis functions are more oscillatory and so a large coefficient c_N for the highest-degree basis function means the solution is quite oscillatory. We make this precise by using the troubled cell indicator presented in [34] for the discontinuous Galerkin method. We define \hat{p}_j as

$$\hat{p}_j(\xi) = c_{j,N} P_N(\xi), \quad (7)$$

i.e. only the highest-degree term in Eq. 3. Then we consider a polynomial admissible if

$$N^{2\alpha_N} \int_{-1}^1 \hat{p}_j^2 d\xi \leq \int_{-1}^1 p_j^2 d\xi, \quad (8)$$

where $\alpha_N = 4$ is generally a good choice since this is when the Legendre basis stops converging [35]. Specifically, this guarantees that the coefficients decay at least as $1/N^2$. We can rewrite the integrals as

$$N^{2\alpha_N} \frac{c_N^2}{2N+1} \leq \sum_{n=0}^N \frac{c_n^2}{2n+1}. \quad (9)$$

This effectively requires that the total power in the highest mode of the Legendre basis expansion is a sufficiently small fraction of the total power. In practice, our PPAO method drops to the next lowest order if Eq. 9 is violated. If the lower-order polynomial violates Eq. 9, the order is dropped again. This is repeated until a second-order scheme, such as monotonized central [36], is used.

We can rewrite the integrals in terms of the primitives directly. For convenience we define

$$\bar{\kappa}_N = \frac{c_N^2}{2N+1}, \quad (10)$$

$$\kappa_N = \sum_{n=0}^N \frac{c_n^2}{2n+1}. \quad (11)$$

Then we write the oscillation indicator at third order as

$$\bar{\kappa}_2 = \frac{2}{5} \left(\frac{3}{4} p_{j+1} - \frac{3}{2} p_j + \frac{3}{4} p_{j-1} \right)^2, \quad (12)$$

$$\kappa_2 = \left(\frac{3}{8} p_{j+1} + \frac{1}{4} p_j + \frac{3}{8} p_{j-1} \right) \left(\frac{31}{20} p_{j+1} - \frac{1}{10} p_j + \frac{11}{20} p_{j-1} \right). \quad (13)$$

The fifth-order terms are given by:

$$\bar{\kappa}_4 = \frac{2}{9} \left(\frac{125}{336} p_{j-2} - \frac{125}{84} p_{j-1} + \frac{125}{56} p_j - \frac{125}{84} p_{j+1} + \frac{125}{336} p_{j+2} \right)^2, \quad (14)$$

$$\begin{aligned} \kappa_4 = & \left(\frac{4015}{12096} p_{j-2} - \frac{925}{3024} p_{j-1} + \frac{2707}{2016} p_j - \frac{2305}{3024} p_{j+1} + \frac{16855}{12096} p_{j+2} \right) \\ & \times \left(\frac{275}{1152} p_{j-2} + \frac{25}{288} p_{j-1} + \frac{67}{192} p_j + \frac{25}{288} p_{j+1} + \frac{275}{1152} p_{j+2} \right). \end{aligned} \quad (15)$$

The seventh-order terms are given by:

$$\begin{aligned} \bar{\kappa}_6 = & \frac{2}{13} \left(\frac{16807}{95040} p_{j-3} - \frac{16807}{15840} p_{j-2} + \frac{16807}{6336} p_{j-1} - \frac{16807}{4752} p_j \right. \\ & \left. + \frac{16807}{6336} p_{j+1} - \frac{16807}{15840} p_{j+2} + \frac{16807}{95040} p_{j+3} \right)^2, \end{aligned} \quad (16)$$

$$\begin{aligned} \kappa_6 = & \left(\frac{52087}{285120} p_{j-3} - \frac{2989}{190080} p_{j-2} + \frac{43757}{95040} p_{j-1} - \frac{72629}{285120} p_j \right. \\ & \left. + \frac{43757}{95040} p_{j+1} - \frac{2989}{190080} p_{j+2} + \frac{52087}{285120} p_{j+3} \right) \times \\ & \left(\frac{748741}{2965248} p_{j-3} - \frac{559769}{1235520} p_{j-2} + \frac{9241603}{4942080} p_{j-1} \right. \\ & \left. - \frac{145879}{57915} p_j + \frac{2928709}{988416} p_{j+1} - \frac{1769887}{1235520} p_{j+2} + \frac{1777657}{1347840} p_{j+3} \right). \end{aligned} \quad (17)$$

The ninth-order terms are given by:

$$\begin{aligned} \bar{\kappa}_8 = & \frac{2}{17} \left(\frac{531441}{6406400} p_{j-4} - \frac{531441}{800800} p_{j-3} + \frac{531441}{228800} p_{j-2} - \frac{531441}{114400} p_{j-1} \right. \\ & \left. + \frac{531441}{91520} p_j - \frac{531441}{114400} p_{j+1} + \frac{531441}{228800} p_{j+2} - \frac{531441}{800800} p_{j+3} \right. \\ & \left. + \frac{531441}{6406400} p_{j+4} \right)^2, \end{aligned} \quad (18)$$

$$\begin{aligned} \kappa_8 = & \left(\frac{62705408397}{243955712000} p_{j-4} - \frac{25040347967}{30494464000} p_{j-3} + \frac{26778669537}{8712704000} p_{j-2} \right. \\ & - \frac{23833259907}{4356352000} p_{j-1} + \frac{25763924917}{3485081600} p_j - \frac{28082791047}{4356352000} p_{j+1} \\ & \left. + \frac{39963815817}{8712704000} p_{j+2} - \frac{54884086987}{30494464000} p_{j+3} + \frac{27239637687}{22177792000} p_{j+4} \right) \times \\ & \left(\frac{9600579}{63078400} p_{j-4} - \frac{673539}{7884800} p_{j-3} + \frac{9532053}{15769600} p_{j-2} \right. \\ & - \frac{508383}{716800} p_{j-1} + \frac{1357457}{1261568} p_j - \frac{508383}{716800} p_{j+1} \\ & \left. + \frac{9532053}{15769600} p_{j+2} - \frac{673539}{7884800} p_{j+3} + \frac{9600579}{63078400} p_{j+4} \right). \end{aligned} \quad (19)$$

2.3. Positivity-preserving strategy

In many physical systems there are requirements on certain variables, for example the density and pressure must remain positive. A few different strategies for maintaining positivity with WENO-type schemes have been presented for Newtonian hydrodynamics[37, 38, 39, 23, 22] and also for ideal non-relativistic MHD[40, 41]. For

more complicated physical systems, such as general relativistic magnetohydrodynamics, generalizations of these strategies are non-trivial or not possible. We seek to ensure that the reconstructed polynomials (6) are physically realizable in a way that is easily tailored to whatever physical constraints are present in the system. While negative densities and pressures could still occur from time integration, this can be avoided by using a positivity-preserving flux limiter [22, 13]. A very simple, efficient, and robust method for preserving positivity in the reconstruction is to check that the cell-face values are positive. If the reconstructed cell-face values are not positive we consider the polynomial to be invalid and switch to a lower-order polynomial. This is repeated until the reconstructed polynomial is positive, which is guaranteed to be true for the first-order scheme.

It is also possible to guarantee that the reconstructed polynomial is positive over the entire region used to construct it. For the fifth-order case this can be done as follows. We can write the *derivative* of the fourth-degree reconstructed polynomial as

$$\partial_{\xi} p_j(\xi) = a\xi^3 + b\xi^2 + c\xi + d, \quad (20)$$

where

$$a = \frac{625}{96} (p_{j-2} - 4p_{j-1} + 6p_j - 4p_{j+1} + p_{j+2}), \quad (21)$$

$$b = \frac{125}{32} (-p_{j-2} + 2p_{j-1} - 2p_{j+1} + p_{j+2}), \quad (22)$$

$$c = -\frac{25}{48} p_{j-2} + \frac{25}{3} p_{j-1} - \frac{125}{8} p_j + \frac{25}{3} p_{j+1} - \frac{25}{48} p_{j+2}, \quad (23)$$

$$d = \frac{5}{24} p_{j-2} - \frac{5}{3} p_{j-1} + \frac{5}{3} p_{j+1} - \frac{5}{24} p_{j+2}. \quad (24)$$

At this point one can use standard methods for finding the roots of a cubic to obtain the ξ coordinates at which the extrema of the reconstructed polynomial occur. If the extrema occur on the interval $[-1, 1]$ one must check that the reconstructed polynomial is positive there. This can be done by using the coefficients computed from Eq. (5) to evaluate the reconstructed polynomial at the extrema and check it is positive.

Rigorously verifying that the entire polynomial is positive is quite expensive, especially for higher than fifth-order reconstruction. An alternative is to evaluate the polynomial at several additional predetermined nodes, similar to [23]. For a linear solution, the extrema occur at the end points so evaluating at the additional nodes $\xi \in \{-1, 1\}$ seems natural. Reasonable additional choices are the cell faces not already required for the Riemann problem. We provide the stencils for evaluating the polynomial at the additional cell faces in table 2. We only write the $\hat{j} - N/2$ coefficients, since the

$\hat{j} + N/2$ coefficients are given by reflecting the stencils about the cell. In practice we have not found evaluating at the additional nodes to be necessary since the coefficients are already decaying as $\sim 1/N^5$ or faster and thus the high frequency components that would lead to large extrema between the nodes are absent. However, this argument does not in principle prevent the end points from being negative. Nevertheless, our current implementation checks for positivity only on the cell-face values, as described in the first paragraph of this subsection, and does not check for positivity at any additional points.

Table 2. Coefficients for reconstructing the polynomials at the additional cell-face values for ensuring positivity of the reconstructed polynomial at different orders. The coefficients for the faces to the right of the cell are obtained by reflecting the coefficients about \hat{j} .

Degree	Face	$\hat{j} - 4$	$\hat{j} - 3$	$\hat{j} - 2$	$\hat{j} - 1$	\hat{j}	$\hat{j} + 1$	$\hat{j} + 2$	$\hat{j} + 3$	$\hat{j} + 4$
2	$\hat{j} - 3/2$				$\frac{15}{8}$	$-\frac{5}{4}$	$-\frac{1}{8}$			
4	$\hat{j} - 5/2$			$\frac{315}{128}$	$-\frac{105}{32}$	$\frac{189}{64}$	$-\frac{45}{32}$	$\frac{35}{128}$		
	$\hat{j} - 3/2$			$\frac{35}{128}$	$\frac{35}{32}$	$-\frac{35}{64}$	$\frac{7}{32}$	$-\frac{5}{128}$		
6	$\hat{j} - 7/2$		$\frac{3003}{1024}$	$-\frac{3003}{512}$	$\frac{9009}{1024}$	$-\frac{2145}{256}$	$\frac{5005}{1024}$	$-\frac{819}{512}$	$\frac{231}{1024}$	
	$\hat{j} - 5/2$		$\frac{231}{1024}$	$\frac{693}{512}$	$-\frac{1155}{1024}$	$\frac{231}{256}$	$-\frac{495}{1024}$	$\frac{77}{512}$	$-\frac{21}{1024}$	
	$\hat{j} - 3/2$		$\frac{21}{1024}$	$\frac{189}{512}$	$\frac{945}{1024}$	$-\frac{105}{256}$	$\frac{189}{1024}$	$-\frac{27}{512}$	$\frac{7}{1024}$	
8	$\hat{j} - 9/2$	$\frac{109395}{32768}$	$-\frac{36465}{4096}$	$\frac{153153}{8192}$	$-\frac{109395}{4096}$	$\frac{425425}{16384}$	$-\frac{69615}{4096}$	$\frac{58905}{8192}$	$-\frac{7293}{4096}$	$\frac{6435}{32768}$
	$\hat{j} - 7/2$	$\frac{6435}{32768}$	$\frac{6435}{4096}$	$-\frac{15015}{8192}$	$\frac{9009}{4096}$	$-\frac{32175}{16384}$	$\frac{5005}{4096}$	$-\frac{4095}{8192}$	$\frac{495}{4096}$	$-\frac{429}{32768}$
	$\hat{j} - 5/2$	$-\frac{429}{32768}$	$\frac{1287}{4096}$	$\frac{9009}{8192}$	$-\frac{3003}{4096}$	$\frac{9009}{16384}$	$-\frac{1287}{4096}$	$\frac{1001}{8192}$	$-\frac{117}{4096}$	$\frac{99}{32768}$
	$\hat{j} - 3/2$	$\frac{99}{32768}$	$-\frac{165}{4096}$	$\frac{3465}{8192}$	$\frac{3465}{4096}$	$-\frac{5775}{16384}$	$\frac{693}{4096}$	$-\frac{495}{8192}$	$\frac{55}{4096}$	$-\frac{45}{32768}$
		$\frac{32768}{32768}$	$-\frac{4096}{4096}$	$\frac{8192}{8192}$	$\frac{4096}{4096}$	$-\frac{16384}{16384}$	$\frac{4096}{4096}$	$-\frac{8192}{8192}$	$\frac{4096}{4096}$	$-\frac{32768}{32768}$

2.4. Finite-difference order adaptation

The final ingredient in our adaptive-order scheme is changing the order of the FD derivative used to approximate the flux divergence in Eq. 2. We must first decide how to take the FD derivative, that is, what nodes to use. In the ECHO scheme presented in [42], a high-order FD derivative is obtained by directly using a fourth-order stencil using the interface numerical fluxes $G_{\hat{j}-3/2}, G_{\hat{j}-1/2}, G_{\hat{j}+1/2}, G_{\hat{j}+3/2}$. Nonomura and Fujii [18] find that using cell-centered fluxes in the FD derivative helps stabilize the scheme, making the conservative FD scheme nearly as robust as FV schemes, while remaining computationally cheaper. For a sixth-order FD derivative Nonomura and Fujii use $G_{\hat{j}-3/2}, F_{\hat{j}-1}, G_{\hat{j}-1/2}, G_{\hat{j}+1/2}, F_{\hat{j}+1}, G_{\hat{j}+3/2}$. This idea was further expanded by Chen, Tóth, and Gombosi [43] (CTG), who use only the nearest cell-interface numerical fluxes and cell-centered fluxes otherwise. For a sixth-order FD derivative CTG use $F_{\hat{j}-2}, F_{\hat{j}-1}, G_{\hat{j}-1/2}, G_{\hat{j}+1/2}, F_{\hat{j}+1}, F_{\hat{j}+2}$. The advantage of using only cell-centered fluxes to

obtain high-order convergence is that this minimizes reconstruction and communication between different processors on a distributed system. CTG also write the high-order FD derivatives as corrections to the numerical flux G . This makes applying a positivity-preserving flux limiter straightforward, unlike if high-order FD derivative stencils are used.

For the above reasons we use the approach taken by CTG, writing the numerical flux G as

$$G_{\hat{j}+1/2} = G_{\hat{j}+1/2}^{(2)} - G_{\hat{j}+1/2}^{(4)} + G_{\hat{j}+1/2}^{(6)} - G_{\hat{j}+1/2}^{(8)} + G_{\hat{j}+1/2}^{(10)}, \quad (25)$$

where $G_{\hat{j}+1/2}^{(2)}$ is the standard numerical flux obtained by solving the Riemann problem at the interface and

$$G_{\hat{j}+1/2}^{(4)} = \frac{1}{6} \left(F_{\hat{j}} - 2G_{\hat{j}+1/2}^{(2)} + F_{\hat{j}+1} \right), \quad (26)$$

$$G_{\hat{j}+1/2}^{(6)} = \frac{1}{180} \left(F_{\hat{j}-1} - 9F_{\hat{j}} + 16G_{\hat{j}+1/2}^{(2)} - 9F_{\hat{j}+1} + F_{\hat{j}+2} \right), \quad (27)$$

$$G_{\hat{j}+1/2}^{(8)} = \frac{1}{2100} \left(F_{\hat{j}-2} - \frac{25}{3}F_{\hat{j}-1} + 50F_{\hat{j}} - \frac{256}{3}G_{\hat{j}+1/2}^{(2)} + 50F_{\hat{j}+1} - \frac{25}{3}F_{\hat{j}+2} + F_{\hat{j}+3} \right), \quad (28)$$

$$G_{\hat{j}+1/2}^{(10)} = \frac{1}{17640} \left(F_{\hat{j}-3} - \frac{49}{5}F_{\hat{j}-2} + 49F_{\hat{j}-1} - 245F_{\hat{j}} + \frac{2048}{5}G_{\hat{j}+1/2}^{(2)} - 245F_{\hat{j}+1} + 49F_{\hat{j}+2} - \frac{49}{5}F_{\hat{j}+3} + F_{\hat{j}+4} \right). \quad (29)$$

We now need to decide which correction orders to include. CTG and Nonomura and Fujii use one order higher than their reconstruction scheme. That is, if fifth-order reconstruction is used, a sixth-order FD derivative is used, which would mean we include $G^{(4)}$ and $G^{(6)}$. We store the polynomial order used for reconstruction in each cell. Then the order we use at $\hat{j} + 1/2$ is given by $\mathcal{O}_{\hat{j}+1/2} = \min(\mathcal{O}_{\hat{j}}, \mathcal{O}_{\hat{j}+1})$, guaranteeing that we do not differentiate across a discontinuity. For example, if cell \hat{j} used fifth-order reconstruction and cell $\hat{j} + 1$ used second-order reconstruction, $G_{\hat{j}+1/2} = G_{\hat{j}+1/2}^{(2)}$.

2.5. Extension to higher dimensions

The extension to higher dimensions is straightforward since for a finite-difference scheme each dimension can be treated separately.

2.6. Weighted adaptive order schemes

We can hybridize the multiple stencils into a single WENO-type stencil, replacing the conditionals by shifted tanh functions. We denote the weight functions for hybridization by $\Theta_{(N)}$ where N is the degree of the scheme. $\Theta_{(N)}$ is one where the stencil should be used and zero where the stencil is invalid. Denoting the stencil of order N by $S^{(N)}$ we write the PPAO9-5-3-1 scheme as:

$$\begin{aligned} p_{j\pm 1/2} &= S_{j\pm 1/2}^{(8)} \Theta_{(8)} \\ &+ (1 - \Theta_{(8)}) \left\{ S_{j\pm 1/2}^{(4)} \Theta_{(4)} \right. \\ &\left. + (1 - \Theta_{(4)}) \left[S_{j\pm 1/2}^{(2)} \Theta_{(2)} + (1 - \Theta_{(2)}) S_{j\pm 1/2}^{(0)} \right] \right\}. \end{aligned} \quad (30)$$

The weight functions based on the oscillation indicators are

$$\Theta_N(s_N^{\hat{j}}; \alpha_N, \gamma) = \frac{1}{1 + \exp(-\gamma s_N^{\hat{j}} + \alpha_N \gamma)}, \quad (31)$$

where γ controls how quickly the transition occurs and should be chosen the same for all stencils. For positivity preservation we use the weight function

$$\Theta_p(S_{j\pm 1/2}^{(N)}; p_{\min}) = \frac{1}{1 + \exp[-(100/p_{\min}) S_{j\pm 1/2}^{(N)} + 50]}, \quad (32)$$

where p_{\min} is the value above which the stencil should be used. That is, if we require the stencil $S^{(N)}$ be used when its value at the reconstruction point is equal to 10^{-13} then $p_{\min} = 10^{-13}$ should be used. When both smoothness and positivity need to be enforced, the weight functions can simply be multiplied together. In this way a general weight function can be obtained that enforces any number of constraints. Finally, the order of the reconstructed polynomial is given by

$$\mathcal{O}_j = 9\Theta_{(8)} + (1 - \Theta_{(8)}) \left\{ 5\Theta_{(4)} + (1 - \Theta_{(4)}) \left[3\Theta_{(2)} + (1 - \Theta_{(2)}) 1 \right] \right\}. \quad (33)$$

3. Numerical results

We now present a series of numerical tests to demonstrate the capabilities of our PPAO schemes. Unless stated otherwise, all tests use a third-order strong-stability-preserving Runge-Kutta scheme (SSP-RK3) for the time evolution[5], and an HLL Riemann solver [44]. We solve the GRMHD equations in conservative form with divergence cleaning. Unless stated otherwise, the second-order reconstruction scheme is monotonized central [36]. See [45] for details of the implementation in **SpECTRE** and [46, 47, 48] for more detailed discussions of the GRMHD system. All simulations are

performed using SpECTRE [49] with the implementation of the algorithms described being publicly available. All features used to perform the simulations described are available in the v2023.04.07 release of SpECTRE [49].

The goal of this section is to get an overview of whether certain choices of reconstruction and FD derivative order are significantly better or worse than others. When comparing schemes we name them both by the PPAO approach and the associated FD derivative approach. PPAO9-5-2-1 means that first unlimited ninth-order reconstruction is attempted, if that fails unlimited fifth-order reconstruction is attempted, if that fails second-order reconstruction is attempted, and if that results in an unphysical solution first-order reconstruction is used. By comparison, PPAO5-2-1 means unlimited fifth-order reconstruction is attempted, if that fails second-order reconstruction is attempted, if that results in an unphysical solution first-order reconstruction is used. When using the same FD derivative order independent of the reconstruction order we use notation like FD-8 for eighth-order FD derivatives, and FD-2 for second-order FD derivatives. When using adaptive-order FD derivatives, we note the order associated with each reconstruction order. For example, if we use PPAO9-5-2-1 with FD-10-6-2-2 (denoted PPAO9-5-2-1+FD-10-6-2-2), then for ninth-order reconstruction we use tenth-order derivatives, for fifth-order reconstruction we use sixth-order derivatives, for second-order reconstruction we use second-order derivatives, and for first-order reconstruction we also use second-order derivatives.

3.1. 1d Smooth Flow

We consider a simple 1d smooth flow problem to verify that the algorithm converges at the expected order for smooth solutions in the absence of magnetic fields. A smooth density perturbation is advected across the domain with a velocity v^i . The analytic solution is given by

$$\rho = 1 + 0.7 \sin[k^i(x^i - v^i t)], \quad (34)$$

$$v^i = (0.8, 0, 0), \quad (35)$$

$$k^i = (1, 0, 0), \quad (36)$$

$$p = 1, \quad (37)$$

$$B^i = (0, 0, 0), \quad (38)$$

and we close the system with an adiabatic equation of state,

$$p = \rho\epsilon(\Gamma - 1), \quad (39)$$

where Γ is the adiabatic index, which we set to 1.4. We use a domain given by $[0, 2\pi]^3$, and apply periodic boundary conditions in all directions. The time step size is $\Delta t = 2\pi/5120$ so that the spatial discretization error is larger than the time stepping error for all resolutions that we use. The final time is chosen to be 2π , and we use a 5th-order Dormand-Prince time integrator [50, 51, 52]. The high-order time stepper combined with the small step size ensure that the spatial errors dominate.

We perform convergence tests at different FD derivative orders and present the results in table 3. We show both the L_2 norm of the error and the convergence rate. The L_2 norm is defined as

$$L_2(u) = \sqrt{\frac{1}{M} \sum_{i=0}^{M-1} u_i^2}, \quad (40)$$

where M is the total number of grid points and u_i is the value of u at grid point i and the convergence order is given by

$$L_2 \text{ Order} = \log_2 \left[\frac{L_2(\mathcal{E}_{N_x/2})}{L_2(\mathcal{E}_{N_x})} \right]. \quad (41)$$

We always use the PPAO9-5-2-1 scheme, but since the solution is smooth ninth-order reconstruction is used. We observe the expected convergence rate except for the 8th-order derivative case, where the convergence order is slightly above the expected rate. This ultimately demonstrates that our PPAO scheme is able to achieve high-order convergence for smooth solutions in the absence of magnetic fields.

3.2. Alfvén Wave

We now verify that our scheme achieves high-order convergence in the presence of magnetic fields. To achieve this we evolve an Alfvén wave across the domain [42]. The magnetic field \mathbf{B} in the Alfvén wave solution is the sum of a background static magnetic field \mathbf{B}_0 and a transverse time-dependent magnetic field \mathbf{B}_1 . We define the auxiliary magnetic velocities v_{B_0} and v_{B_1} as

$$v_{B_0}^2 = \frac{(B_0)^2}{\rho h + B^2}, \quad v_{B_1}^2 = \frac{(B_1)^2}{\rho h + B^2}. \quad (42)$$

The Alfvén speed and fluid speed are then given by:

$$v_A^2 = \frac{v_{B_0}^2}{\frac{1}{2} + \sqrt{\frac{1}{4} - v_{B_0}^2 v_{B_1}^2}}, \quad v_f^2 = \frac{v_{B_1}^2}{\frac{1}{2} + \sqrt{\frac{1}{4} - v_{B_0}^2 v_{B_1}^2}}. \quad (43)$$

Table 3. The errors and local convergence order for the smooth flow problem using different FD derivative orders but always using a PPAO9-5-2-1 reconstruction. Since the solution is smooth the reconstruction always ends up being 9th order. We observe the expected convergence rate except for the 8th-order derivative it is slightly higher than expected.

Derivative Order	N_x	$L_2(\mathcal{E}(\rho))$	L_2 Order
2	11	2.41440e-2	
	22	6.04972e-3	2.00
	44	1.51327e-3	2.00
	88	3.78368e-4	2.00
4	11	2.81416e-4	
	22	1.76480e-5	4.00
	44	1.10441e-6	4.00
	88	6.90479e-8	4.00
6	11	7.40386e-6	
	22	9.86855e-8	6.23
	44	1.53525e-9	6.01
	88	2.39498e-11	6.00
8	11	3.25675e-6	
	22	6.79011e-9	8.91
	44	1.37058e-11	8.95
	88	1.19152e-13	6.85
10	11	3.27319e-6	
	22	6.79768e-9	8.91
	44	1.35104e-11	8.97
	88	1.15890e-13	6.87
10-6-2-2	11	3.27319e-6	
	22	6.79768e-9	8.91
	44	1.35104e-11	8.97
	88	1.15890e-13	6.87
10-4-2-2	11	3.27319e-6	
	22	6.79768e-9	8.91
	44	1.35104e-11	8.97
	88	1.15890e-13	6.87

We use an ideal fluid equation of state with $\Gamma = 1.6$

The circularly polarized wave is best described in a basis aligned with the initial magnetic fields at the origin. To this end we define the unit vectors $\hat{\mathbf{b}}_0$, $\hat{\mathbf{b}}_1$, and $\hat{\mathbf{e}}$ as

$$\hat{\mathbf{b}}_0 = \frac{\mathbf{B}_0}{B_0}, \quad \hat{\mathbf{b}}_1 = \frac{\mathbf{B}_1}{B_1} \Big|_{\mathbf{x}=\mathbf{0}, t=0}, \quad \hat{\mathbf{e}} = \hat{\mathbf{b}}_0 \times \hat{\mathbf{b}}_1. \quad (44)$$

The analytic solution is given by

$$\mathbf{v}(\mathbf{x}, t) = -v_f \left[\cos(\delta\phi) \hat{\mathbf{b}}_1 + \sin(\delta\phi) \hat{\mathbf{e}} \right], \quad (45)$$

$$\mathbf{B}(\mathbf{x}, t) = \mathbf{B}_0 + B_1 \left[\cos(\delta\phi) \hat{\mathbf{b}}_1 + \sin(\delta\phi) \hat{\mathbf{e}} \right], \quad (46)$$

with $\delta\phi$ given by

$$\delta\phi(\mathbf{x}, t) = k \left(\mathbf{x} \cdot \hat{\mathbf{b}}_0 - v_A t \right), \quad (47)$$

where k is the wave number, and ρ and p are spatially constant. We choose $\rho = 1$, $p = 1$, $k = \sqrt{3}$, $\mathbf{B}_0 = [1, 1, 1]$, and $\mathbf{B}_1(\mathbf{0}, 0) = [\sqrt{2}, -1/\sqrt{2}, -1/\sqrt{2}]$.

We use an adaptive Dormand-Prince 5 [50, 51, 52] time integrator with an absolute tolerance of 10^{-15} and a relative tolerance of 10^{-13} , and evolve to a final time of π . In table 4 we present convergence results of B^i at the final time. We always use the PPAO9-5-2-1 scheme, but since the solution is smooth, ninth-order reconstruction is used. From table 4 we see that we get high-order convergence for the Alfvén wave problem, though when using tenth-order FD derivatives we still only achieve eighth-order convergence. We have not yet understood why this is, though given the time stepper tolerance and the small errors, we are not concerned about it. In realistic astrophysical simulations one is highly unlikely to be able to achieve relative errors of 10^{-12} .

3.3. 1d Riemann Problems

Having verified the order of convergence of our PPAO scheme for smooth solutions, we now turn to testing them in the presence of discontinuities. One-dimensional Riemann problems are a standard test for any scheme that must be able to handle shocks. We will focus on the five Riemann problems (RP-5) of [53] and the fast shock problem of [54]. The initial conditions for the Riemann problems are given in table 5. We use a domain given by $[-0.5, 0.5] \times [-1, 1]^2$, with 704 grid points in the x -direction and 11 grid points in y and z , analytic boundary conditions in the x -direction and periodic in y and z , and use a time step size $\Delta t = 5 \times 10^{-4}$. The initial conditions for the fast shock are given by [54]

$$\rho = \begin{cases} 1.0, & \text{if } x \leq 0.0 \\ 25.48, & x > 0.0, \end{cases} \quad (48)$$

$$p = \begin{cases} 1.0, & \text{if } x \leq 0.0 \\ 367.5, & x > 0.0, \end{cases} \quad (49)$$

$$B^i = \begin{cases} (20.0, 25.02, 0.0), & \text{if } x \leq 0.0 \\ (20.0, 49.0, 0.0), & x > 0.0, \end{cases} \quad (50)$$

$$u^i = \begin{cases} (25.0, 0.0, 0.0), & \text{if } x \leq 0.0 \\ (1.091, 0.392, 0.0), & x > 0.0, \end{cases} \quad (51)$$

Table 4. The errors and local L_2 convergence order for the Alfvén wave problem using different FD derivative orders but always using a PPAO9-5-2-1 reconstruction. We show the error and order for each component of the magnetic field separately, and in all cases observe high-order convergence. We have not yet understood why the tenth-order derivatives only converge at eighth order, though given the time stepper tolerance and the small errors, we are not concerned about it.

$\mathcal{O}(\text{FD})$	N_x	$L_2(\mathcal{E}(B^x))$	$\mathcal{O}(B_x)$	$L_2(\mathcal{E}(B^y))$	$\mathcal{O}(B^y)$	$L_2(\mathcal{E}(B^z))$	$\mathcal{O}(B^z)$
2	22	1.08968e-2		1.08968e-2		1.08968e-2	
	44	2.72631e-3	2.00	2.72631e-3	2.00	2.72631e-3	2.00
	88	6.81709e-4	2.00	6.81709e-4	2.00	6.81709e-4	2.00
4	22	4.43192e-5		4.43192e-5		4.43192e-5	
	44	2.77829e-6	4.00	2.77829e-6	4.00	2.77829e-6	4.00
	88	1.73745e-7	4.00	1.73745e-7	4.00	1.73745e-7	4.00
6	22	3.10693e-7		3.10693e-7		3.10693e-7	
	44	4.95066e-9	5.97	4.95066e-9	5.97	4.95066e-9	5.97
	88	7.89883e-11	5.97	7.89881e-11	5.97	7.89882e-11	5.97
8	22	1.45926e-7		1.45926e-7		1.45926e-7	
	44	5.66948e-10	8.01	5.66949e-10	8.01	5.66949e-10	8.01
	88	5.58414e-12	6.67	5.58425e-12	6.67	5.58425e-12	6.67
10	22	1.49272e-7		1.49272e-7		1.49272e-7	
	44	5.80746e-10	8.01	5.80746e-10	8.01	5.80745e-10	8.01
	88	5.63870e-12	6.69	5.63867e-12	6.69	5.63866e-12	6.69
10-6-2-2	22	1.49272e-7		1.49272e-7		1.49272e-7	
	44	5.80746e-10	8.01	5.80746e-10	8.01	5.80745e-10	8.01
	88	5.63870e-12	6.69	5.63867e-12	6.69	5.63866e-12	6.69
10-4-2-2	22	1.49272e-7		1.49272e-7		1.49272e-7	
	44	5.80746e-10	8.01	5.80746e-10	8.01	5.80745e-10	8.01
	88	5.63870e-12	6.69	5.63867e-12	6.69	5.63866e-12	6.69

(52)

using a domain $[-0.5, 2] \times [-1, 1]^2$ with 352 grid points in the x -direction and 11 grid points in y and z , analytic boundary conditions in all directions, and we use a time step size of $\Delta t = 10^{-3}$.

We plot the rest mass density ρ at the final time in the left panels of figure 1 and figure 2, and the y -component of the magnetic field B^y at the final time in the right panels for the various Riemann problems and the fast shock problem. The PPAO9-5-2-1 reconstruction scheme is always used and different FD derivative orders are shown. We find that FD-8 fails for RP4, while both FD-2 and the adaptive FD-10-6-2-2 are robust. For RP3, we see that the adaptive-order FD derivatives leads to larger oscillations in B^y around $x = 0.35$ than the FD-8 scheme. This is because the FD-8 scheme is more dissipative than the adaptive approach, and so there is essentially a low-pass filter applied that smooths out additional oscillations, be they physical or unphysical. In all

Table 5. The initial conditions for Riemann Problems 1, 2, 3, 4, and 5 of [53]. The domain is $x \in [-0.5, 0.5]$, the final time is $t_f = 0.4$ for problems 1–4 and $t_f = 0.55$ for problem 5. An ideal fluid equation of state is used with an adiabatic index of 2 for Riemann Problem 1 and 5/3 for Riemann Problems 2, 3, 4, and 5.

Problem		ρ	p	v^i	B^i
RP 1	$x < 0$	1.0	1.0	(0.0 , 0.0, 0.0)	(0.5, 1.0, 0.0)
	$x \geq 0$	0.125	0.1	(0.0 , 0.0, 0.0)	(0.5, -1.0, 0.0)
RP 2	$x < 0$	1.0	30.0	(0.0 , 0.0, 0.0)	(5.0, 6.0, 6.0)
	$x \geq 0$	1.0	1.0	(0.0 , 0.0, 0.0)	(5.0, 0.7, 0.7)
RP 3	$x < 0$	1.0	1000.0	(0.0 , 0.0, 0.0)	(10.0, 7.0, 7.0)
	$x \geq 0$	1.0	0.1	(0.0 , 0.0, 0.0)	(10.0, 0.7, 0.7)
RP 4	$x < 0$	1.0	0.1	(0.999, 0.0, 0.0)	(10.0, 7.0, 7.0)
	$x \geq 0$	1.0	0.1	(-0.999, 0.0, 0.0)	(10.0, -7.0, -7.0)
RP 5	$x < 0$	1.08	0.95	(0.4 , 0.3, 0.2)	(2.0, 0.3, 0.3)
	$x \geq 0$	1.0	1.0	(-0.45 , -0.2, 0.2)	(2.0, -0.7, 0.5)

cases we see that adapting the order of the FD derivative increases accuracy without additional Gibbs phenomena or decreased shock capturing compared to the second-order scheme. This demonstrates that the combined PPAO9-5-2-1+FD-10-6-2-2 scheme is able to achieve high-order convergence in smooth regions while accurately and robustly capturing strong shocks and discontinuities, at least for 1d test problems. We explore the scheme’s capabilities of handling 2d and 3d problems below.

3.4. 2d Cylindrical Blast Wave

The cylindrical blast wave [55, 42] is a standard test problem in which a magnetized fluid obeying a $\Gamma = 4/3$ ideal fluid equation of state starts at rest in a constant magnetic field along the x -axis is evolved. A dense cylinder is surrounded by a lower density fluid into which the cylinder expands. The presence of a magnetic field causes the expansion to be non-axially symmetric. The initial density ρ and pressure p of the fluid are

$$\rho(r < 0.8) = 10^{-2}, \quad (53)$$

$$\rho(r > 1.0) = 10^{-4}, \quad (54)$$

$$p(r < 0.8) = 1, \quad (55)$$

$$p(r > 1.0) = 5 \times 10^{-4}. \quad (56)$$

In the region $0.8 \leq r \leq 1$, the solution transitions such that the logarithms of the pressure and density are linear functions of r . The fluid begins threaded with a magnetic

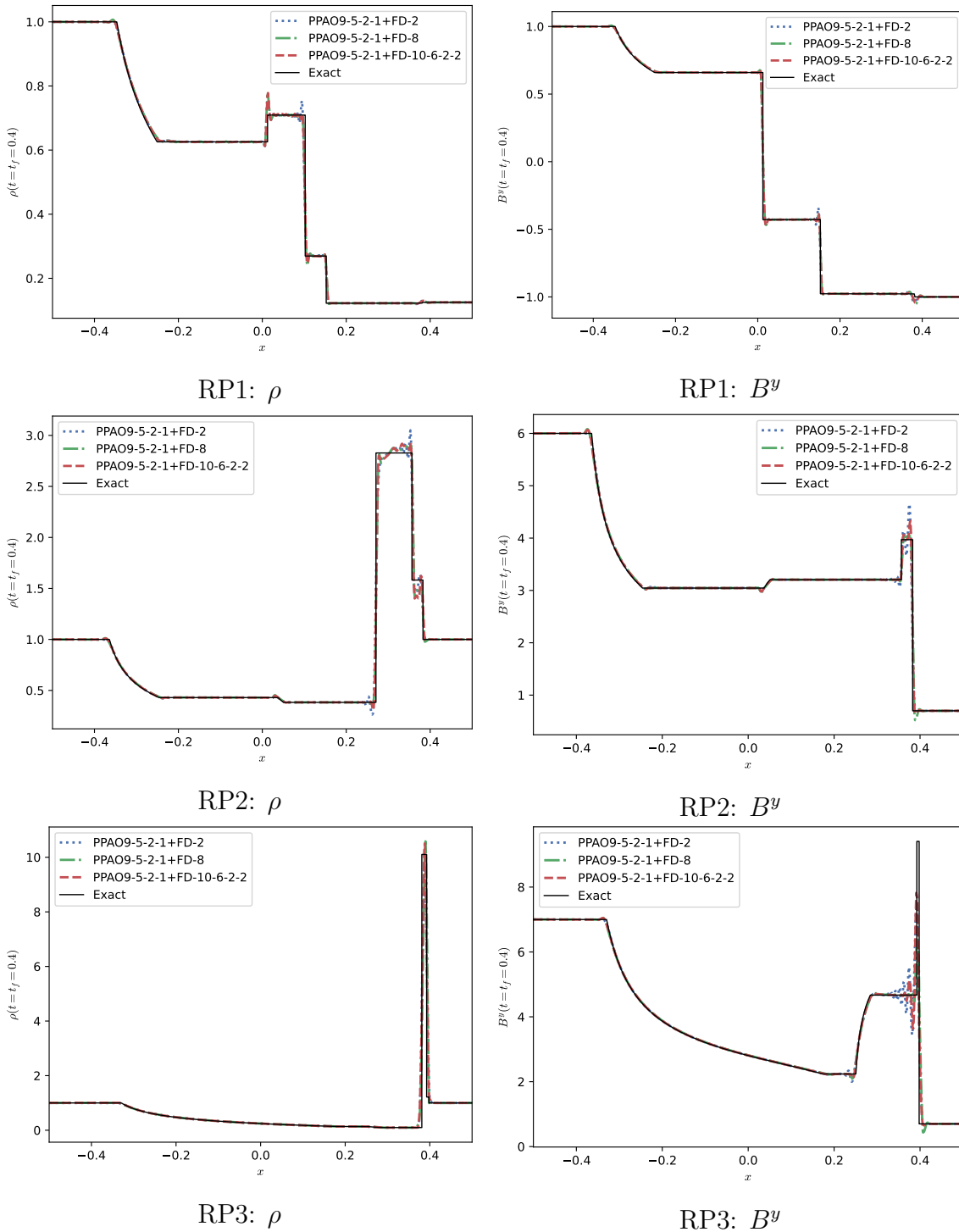


Figure 1. The left panels show the rest mass density ρ at the final for Riemann problems 1-3 going from top to bottom, while the right panel shows B^y at the final time. In all cases we show the exact solution in solid black and our PPAO-9-5-2-1 scheme with different derivative orders. We see that for all three Riemann problems the adaptive-order derivatives provide the best balance between accurately resolving shocks and minimizing oscillations near discontinuities.

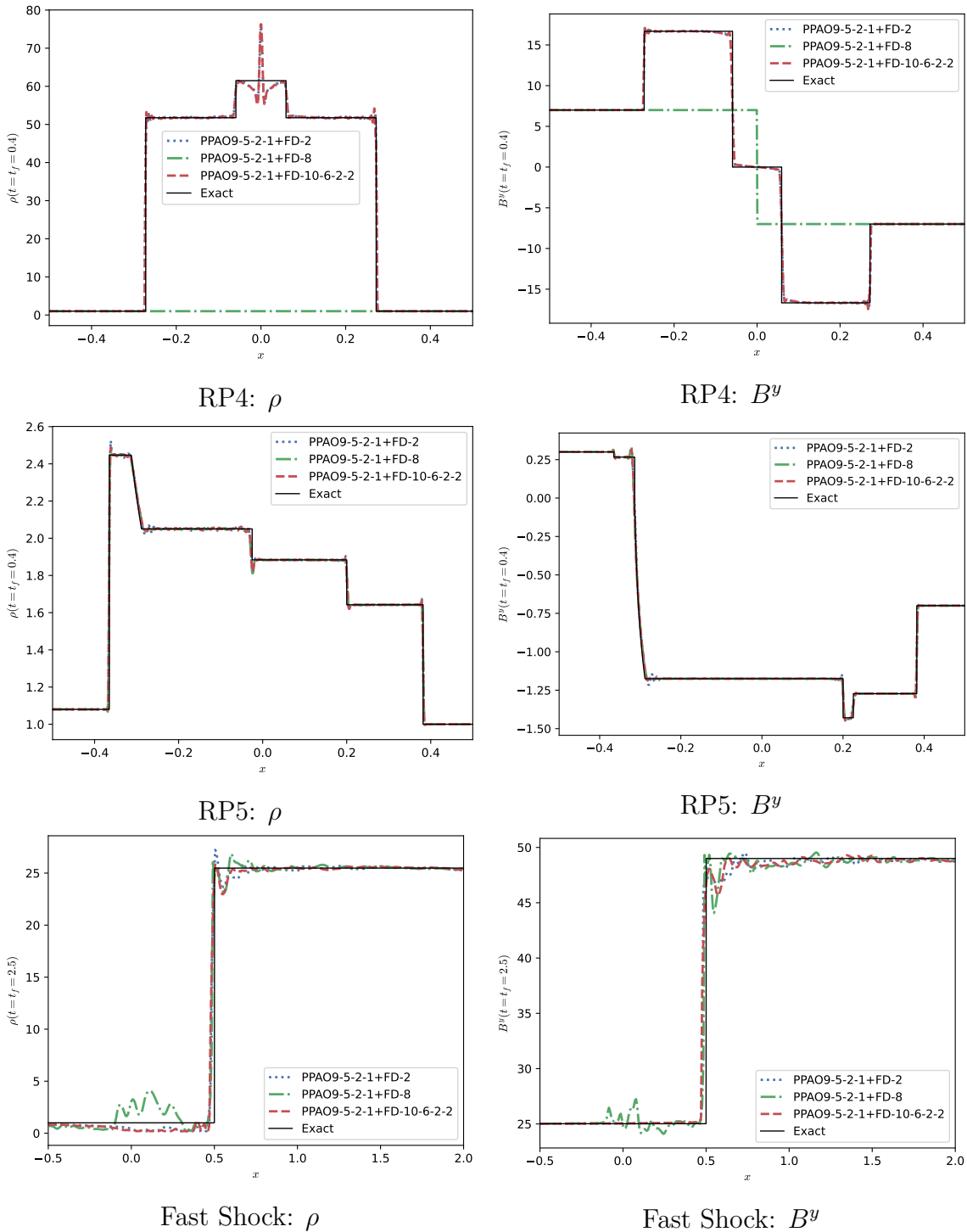


Figure 2. The left panels show the rest mass density ρ at the final for Riemann problems 4-5 and the Komissarov fast shock going from top to bottom, while the right panel shows B^y at the final time. In all cases we show the exact solution in solid black and our PPAO-9-5-2-1 scheme with different derivative orders. The FD-8 solver fails for RP4 and does quite poorly for the fast shock problem. In all cases the adaptive order scheme is accurate and robust.

field:

$$(B^x, B^y, B^z) = (0.1, 0, 0). \quad (57)$$

For all simulations we use a time step size $\Delta t = 10^{-2}$.

We evolve the blast wave to time $t_f = 4.0$ using a $240 \times 240 \times 15$ FD grid on a cubical domain of size $[-6, 6]^3$ and apply periodic boundary conditions in all directions. We show the logarithm of the rest mass density ρ at t_f in figure 3 for different FD derivative orders but always using the PPAO9-5-2-1 reconstruction method. We label the panels FD- N , where N is the FD derivative order. The 10-6-2-2 and 10-4-2-2 use tenth-order FD derivatives when ninth-order reconstruction is used, sixth (fourth) order derivatives when fifth-order reconstruction is used, and second-order derivatives when first- and second-order reconstruction is used. Despite the high-order nature of the method, it is able to robustly capture the sharp features that arise, demonstrating that the scheme robustly detects discontinuities and reduces the reconstruction order in so as to remain stable. We show the reconstruction order alongside ρ and pressure p in figure 4. In this case discontinuous features in ρ and p are at the spatial locations and the scheme correctly identifies them. A similar plot for the Kelvin-Helmholtz instability discussed below (§ 3.7) shows that the code can track both shocks and contact discontinuities.

A particularly challenging case is when the initial magnetic field is increased to $B^x = 0.5$, as was done in [56]. In this case we must use minmod reconstruction [57] at second order instead of monotized central in order for the simulations to remain stable, but the PPAO scheme is otherwise able to evolve the solution without any challenges. We show results analogous to the weaker field case in figure 5.

3.5. 2d Magnetic Rotor

The 2d magnetic rotor problem was first proposed for non-relativistic MHD [58, 59] and later generalized to the relativistic case [60, 61]. A rotating cylinder of dense fluid is surrounded by a lower density fluid, with uniform pressure and magnetic field. Magnetic braking ultimately slows the rotor and an approximately 90 degree rotation is completed by the final time $t_f = 0.4$. We set up the problem on a $272 \times 272 \times 17$ grid with domain size $[-0.5, 0.5]^3$, periodic boundary conditions in all directions, and a time step size $\Delta t = 10^{-3}$. A $\Gamma = 5/3$ ideal fluid equation of state is used with initial conditions:

$$p = 1 \quad (58)$$

$$B^i = (1, 0, 0) \quad (59)$$

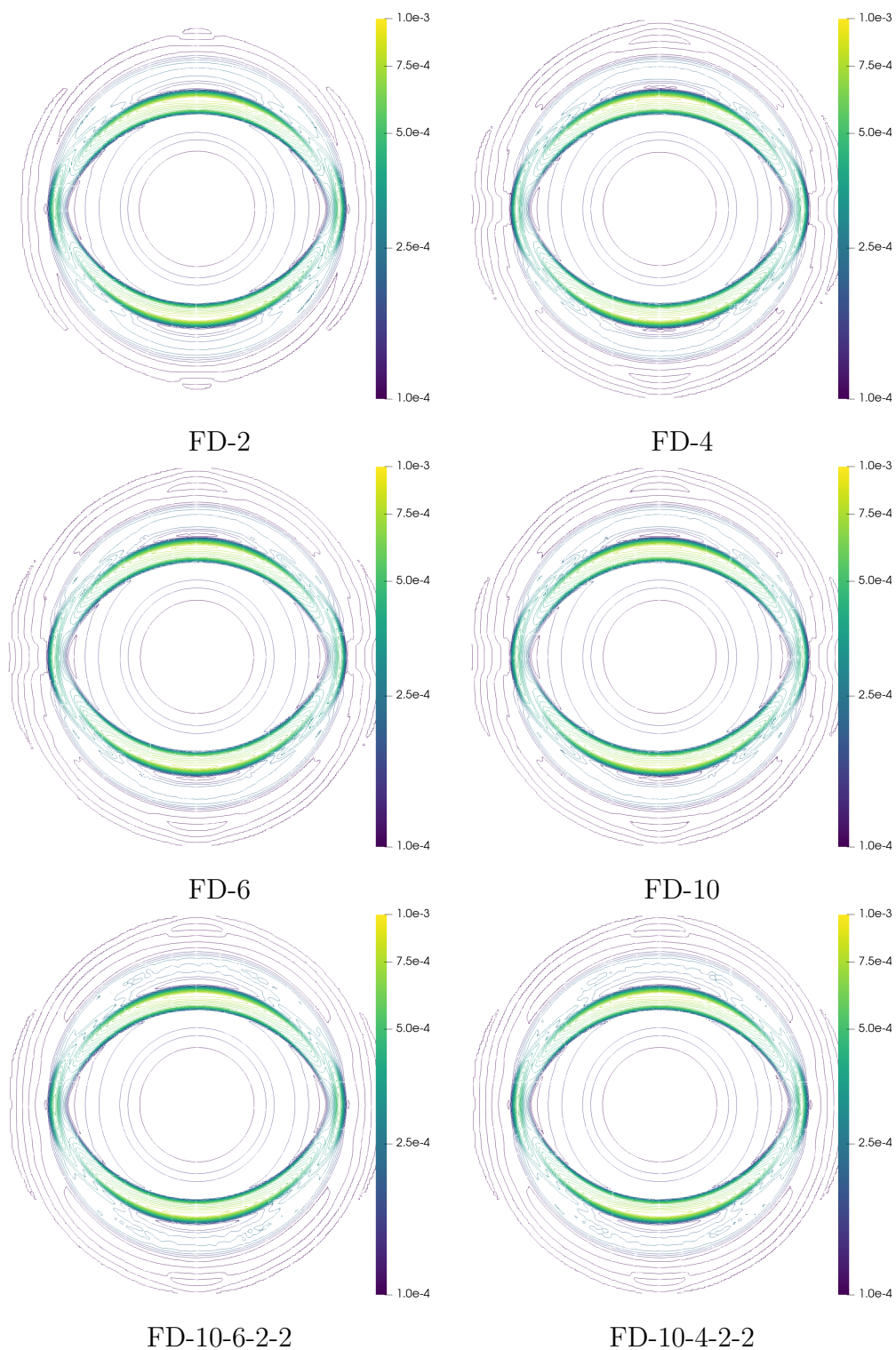


Figure 3. Cylindrical blast wave ρ at $t = 4$ showing the results using different FD derivative orders and always using the PPAO9-5-2-1 reconstruction method. In all cases the scheme is stable, meaning we are able to achieve high-order in smooth regions while being robust and stable at discontinuities and shocks. In all cases the scheme is stable. There are 30 contours linearly spaced between 10^{-3} and 10^{-4} .

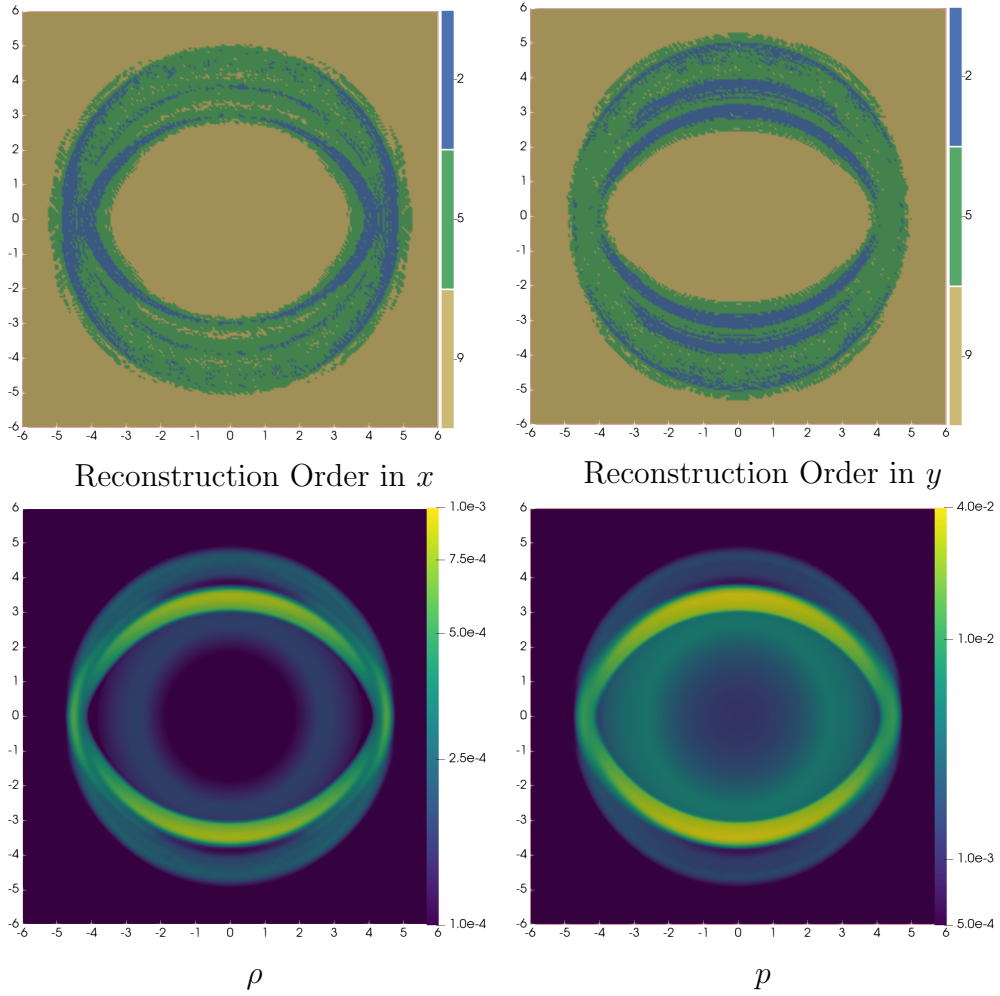


Figure 4. Results from the cylindrical blast wave problem. The panels in the top row show the reconstruction and FD derivative order used in the x -direction (left) and y -direction (right) at the final time, while the bottom left panel shows the rest mass density and the bottom right the pressure at the final time. We see that the adaptive-order FD scheme accurately tracks non-smooth features in the solution, specifically the rest mass density and pressure, adjusting the order as necessary.

$$v^i = \begin{cases} (-y\Omega, x\Omega, 0), & \text{if } r \leq R_{\text{rotor}} = 0.1 \\ (0, 0, 0), & \text{otherwise,} \end{cases} \quad (60)$$

$$\rho = \begin{cases} 10, & \text{if } r \leq R_{\text{rotor}} = 0.1 \\ 1, & \text{otherwise,} \end{cases} \quad (61)$$

where $\Omega = 9.95$ is the angular velocity, guaranteeing that the maximum velocity of the fluid (0.995) is below the speed of light.

We show the results of our evolutions in figure 6. Again, we label the panels FD- N , where N is the FD derivative order. The 10-6-2-2 and 10-4-2-2 use tenth-order FD derivatives when ninth-order reconstruction is used, sixth (fourth) order derivatives

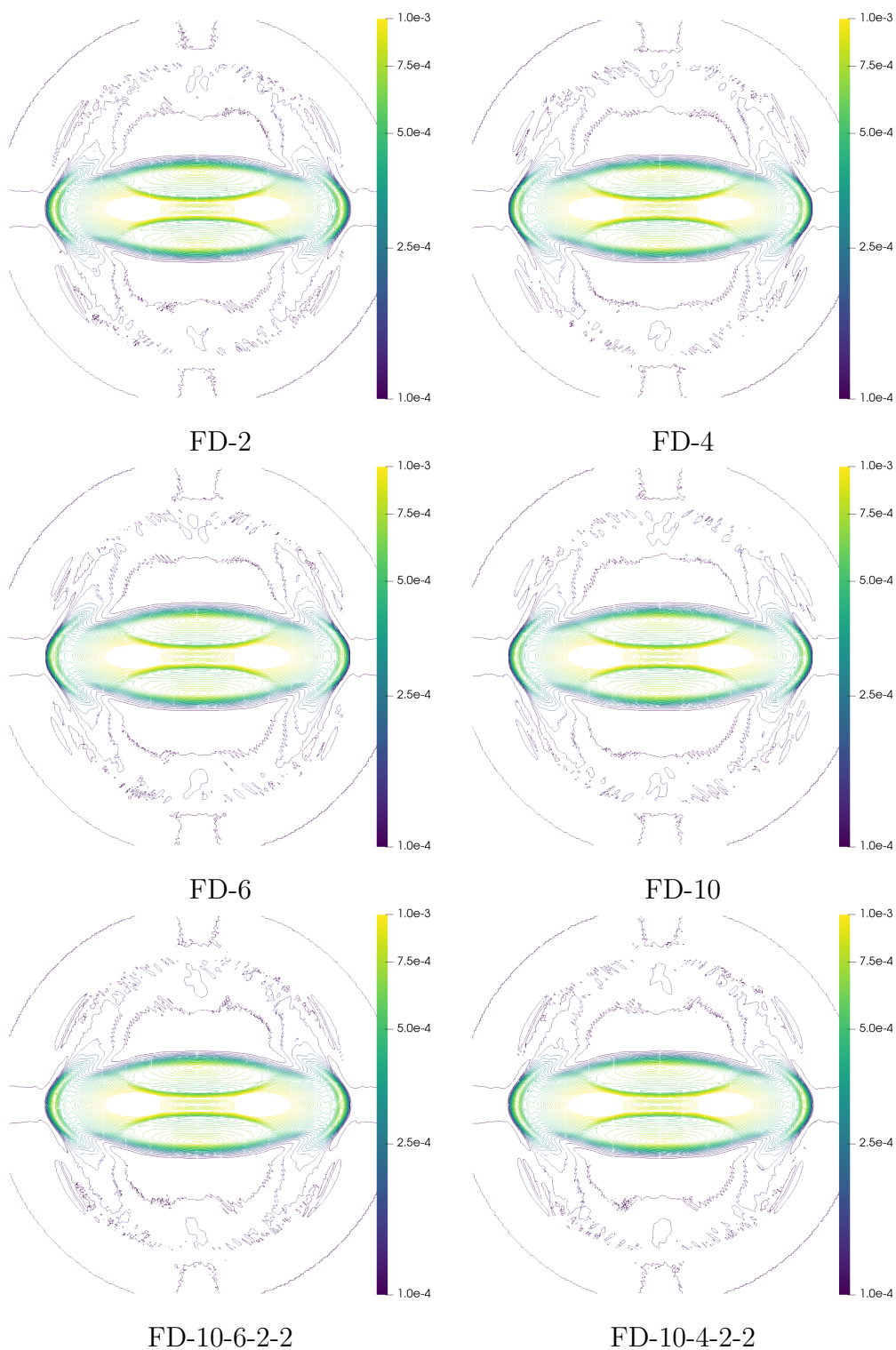


Figure 5. Strongly magnetized ($B^x = 0.5$) cylindrical blast wave ρ at $t = 4$ showing the results using different FD derivative orders and always using the PPA09-5-2-1 reconstruction method, where at second order minmod reconstruction is used. In all cases the scheme is stable. There are 30 contours linearly spaced between 10^{-3} and 10^{-4} .

when fifth-order reconstruction is used, and second-order derivatives when first- and second-order reconstruction is used. Just as in the cylindrical blast wave test case, our adaptive order scheme is able to robustly evolve the discontinuous parts of the solution while maintaining high order where the solution is smooth.

3.6. 2d Magnetic Loop Advection

The 2d magnetic loop advection problem [62] gives a nice test of how well the method is able to advect magnetic fields through the domain, and if the divergence cleaning is working properly. In this problem, a magnetic loop is advected through the domain until it returns to its starting position. We use an initial configuration very similar to [63, 64, 65, 66], where

$$\rho = 1 \tag{62}$$

$$p = 3 \tag{63}$$

$$v^i = (1/1.2, 1/2.4, 0) \tag{64}$$

$$B^x = \begin{cases} -A_{\text{loop}}y/R_{\text{in}}, & \text{if } r \leq R_{\text{in}} \\ -A_{\text{loop}}y/r, & \text{if } R_{\text{in}} < r < R_{\text{loop}} \\ 0, & \text{otherwise,} \end{cases} \tag{65}$$

$$B^y = \begin{cases} A_{\text{loop}}x/R_{\text{in}}, & \text{if } r \leq R_{\text{in}} \\ A_{\text{loop}}x/r, & \text{if } R_{\text{in}} < r < R_{\text{loop}} \\ 0, & \text{otherwise,} \end{cases} \tag{66}$$

with $R_{\text{loop}} = 0.3$, $R_{\text{in}} = 0.001$, $A_{\text{loop}} = 10^{-3}$ and an ideal gas equation of state with $\Gamma = 5/3$. The FD grid is $240 \times 240 \times 15$ and the domain size is $[-0.5, 0.5]^3$ with periodic boundary conditions. We use a time step size of $\Delta t = 10^{-3}$ and evolve to a final time of $t_f = 2.4$, one period.

In the left half of each plot in figure 7 we plot B^x at $t = 0$, while in the right half we plot B^x at $t_f = 2.4$. If the numerical method perfectly preserved the structure the two halves would look identical. However, we see that using second-order derivatives everywhere (top left panel) creates additional oscillations in the cone that are not present when high-order (labeled FD-4, FD-6, and FD-10) or adaptive-order (labeled FD-10-6-2-2 and FD-10-4-2-2) derivatives are used. We show the divergence cleaning field Φ in figure 8, which is a direct measure of the $\partial_i B^i = 0$ constraint violation. We see that in addition to a random background, the high-order derivatives have larger constraint violations

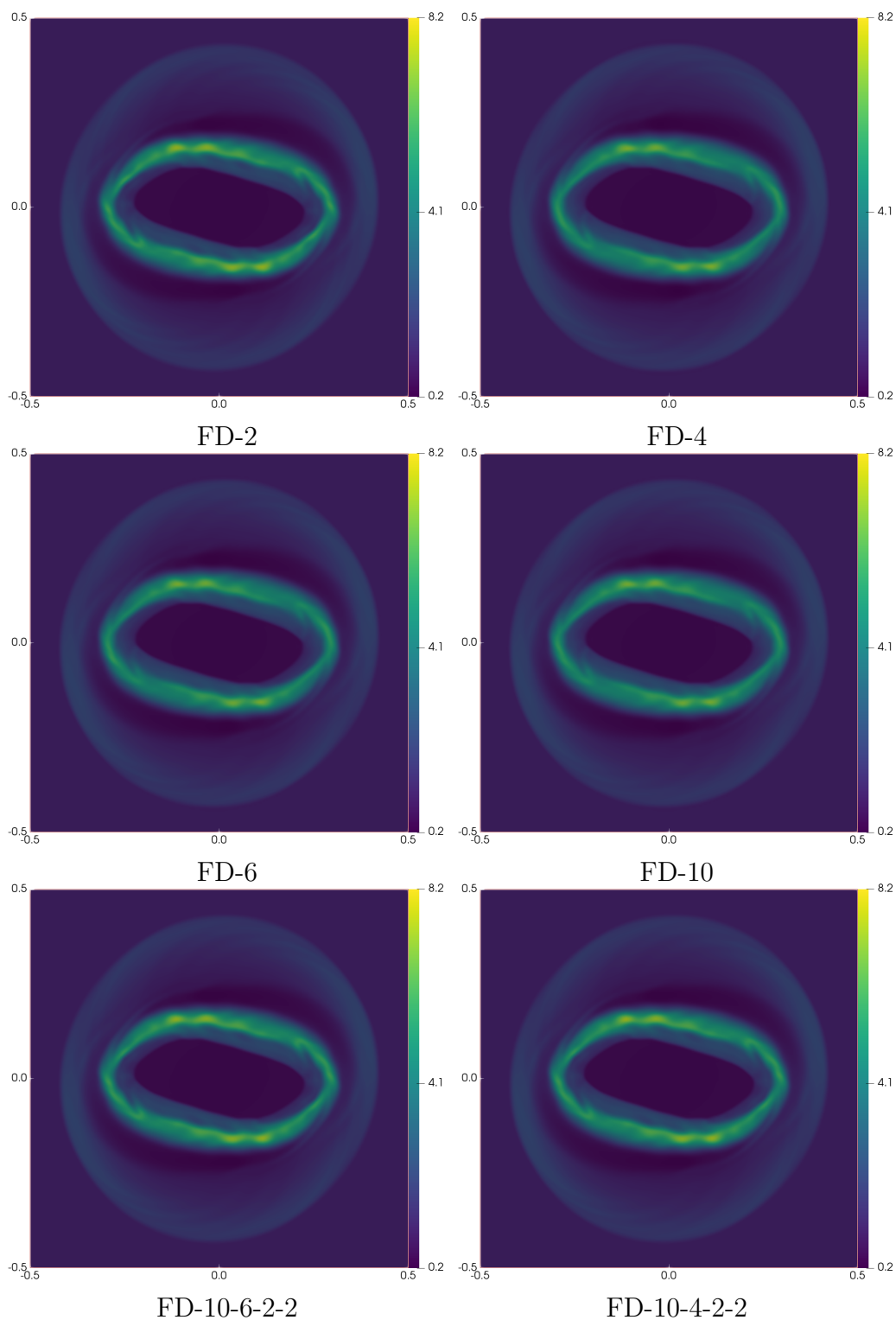


Figure 6. Magnetic rotor ρ at $t = 0.45$ showing the results using different FD derivative orders and always using the PPAO9-5-2-1 reconstruction method. In all cases the scheme is stable, meaning we are able to achieve high-order in smooth regions while being robust and stable at discontinuities and shocks.

at the outer edge of the loop ($r = R_{\text{loop}} = 0.3$). However, the violations at R_{loop} are still of the same scale as the background violations and so do not adversely affect the overall solution. This demonstrates that our high-order and adaptive-order methods do not adversely affect the divergence cleaning properties of the GRMHD system.

3.7. Kelvin-Helmholtz instability

Next we study a magnetized Kelvin-Helmholtz (KH) instability, similar to [67]. The domain is $[-0.5, 0.5]^3$, periodic boundary conditions are applied in all directions, and we use initial conditions similar to [68]:

$$\rho = \begin{cases} 1, & |y - 0.5| < 0.25 \\ 10^{-2}, & \text{otherwise,} \end{cases} \quad (67)$$

$$p = 1.0, \quad (68)$$

$$v^x = \begin{cases} 0.5, & |y - 0.5| < 0.25 \\ -0.5, & \text{otherwise,} \end{cases} \quad (69)$$

$$v^y = 0.1 \sin(4\pi x) \left[\exp\left(-\frac{(y - 0.75)^2}{0.0707^2}\right) + \exp\left(-\frac{(y - 0.25)^2}{0.0707^2}\right) \right], \quad (70)$$

$$v^z = 0.0, \quad (71)$$

$$B^i = (10^{-3}, 0, 0). \quad (72)$$

An ideal gas equation of state is used with $\Gamma = 4/3$ and simulation to a final time $t_f = 1.6$ with a CFL factor of 0.7. We find that using second-order FD derivatives and the adaptive-order derivatives the simulations are stable with a CFL of 0.9, while derivatives orders four through ten are unstable with such a large CFL.

We plot the rest mass density ρ from a high-resolution, 1408^2 , reference simulation using PPAO9-5-2-1 and FD-2 in figure 9 to compare our results to. The high-resolution simulation has four times as many points per dimension as our standard resolution. We plot the rest mass density ρ at the final time $t_f = 1.6$ in figure 10 for simulations using the PPAO9-5-2-1 reconstruction scheme but using different order FD derivatives. All schemes are stable, though the FD-2 is able to resolve additional small-scale vortices at $(x, y) \sim (0.5, 0.25)$ and FD-10-6-2-2 is almost able to resolve these. We find that reducing the CFL factor to 0.5 allows the FD-10-6-2-2 scheme to resolve the additional vortices, similar to those seen in the high-resolution simulation shown in figure 9. We show the reconstruction order alongside ρ and pressure p in figure 11, nicely demonstrating that the PPAO scheme accurately tracks non-smooth features in both ρ and p . This ultimately

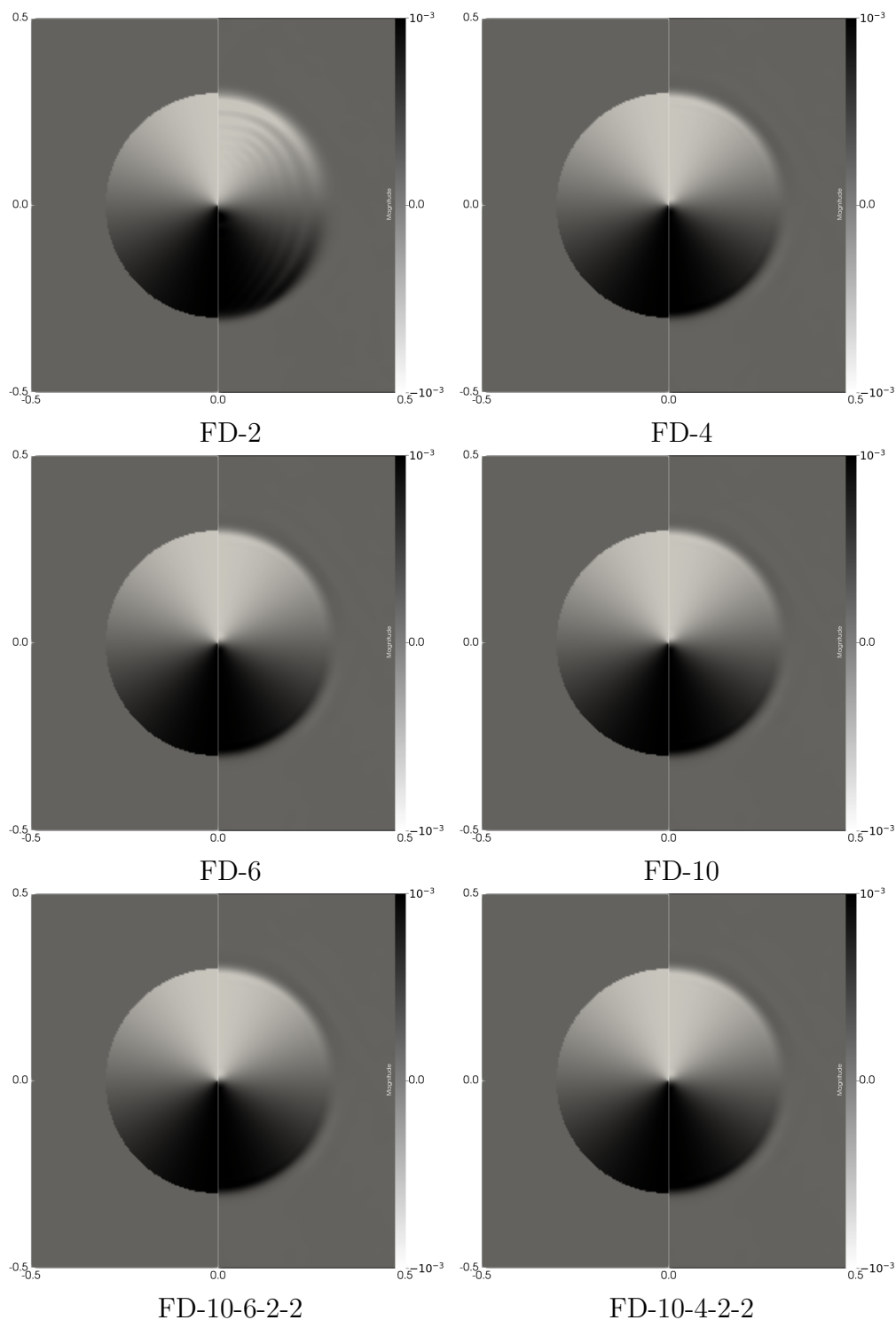


Figure 7. B^x for the magnetic loop advection problem. The left half of each plot is at the initial time, while the right half is after one period ($t_f = 2.4$). The different panels all use the same PPAO9-5-2-1 reconstruction method but use different derivative orders. We see that the second-order FD derivative generates spurious oscillations throughout the loop, while the high-order and adaptive-order FD derivatives produce a cleaner solution.

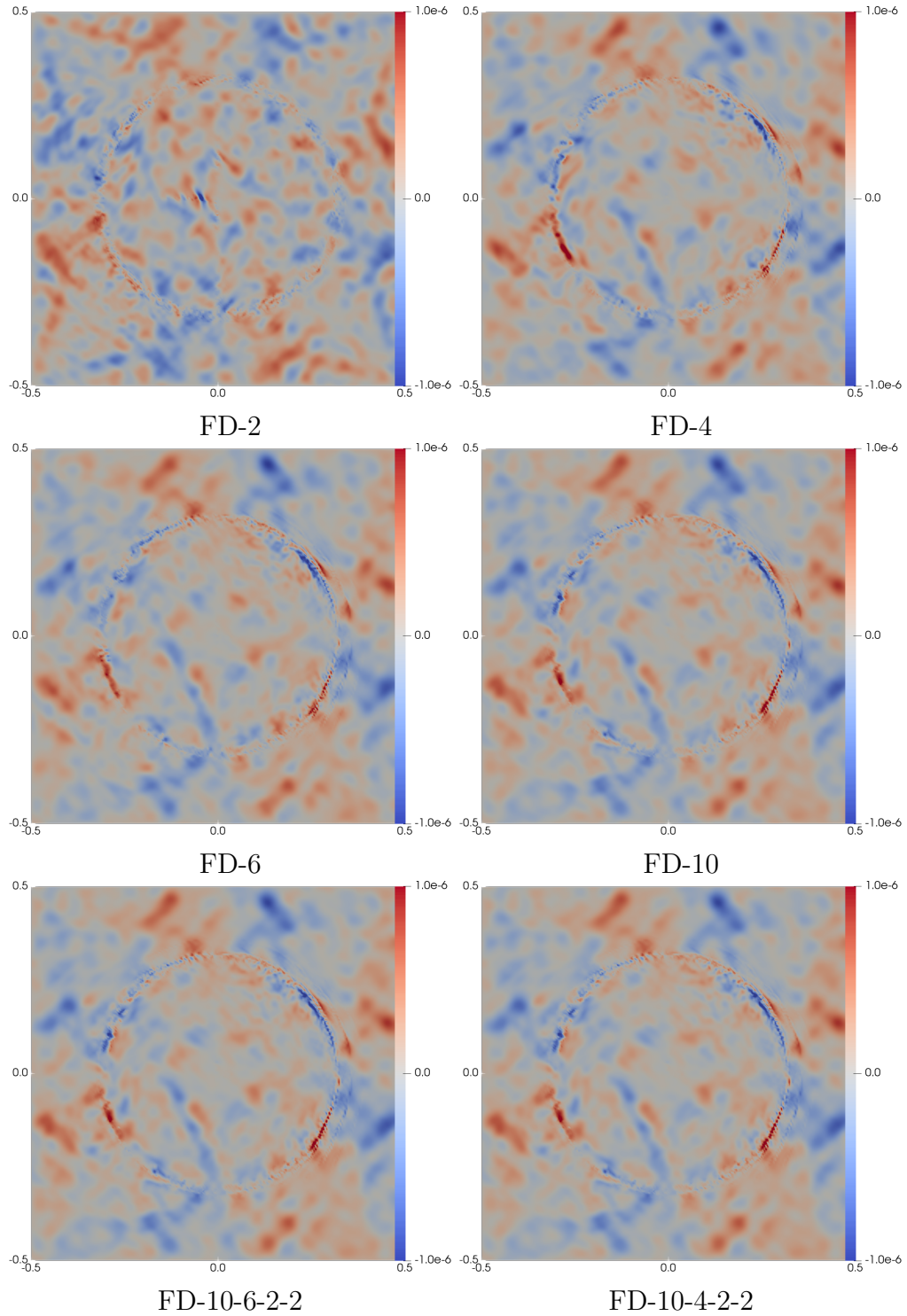


Figure 8. The divergence cleaning field Φ for the magnetic loop advection problem after one period ($t_f = 2.4$). The different panels all use the same PPAO9-5-2-1 reconstruction method but use different derivative orders. We see that high-order FD derivatives generate additional $\partial_i B^i = 0$ constraint violations at the edge of the loop, but at an amplitude comparable to that of the background noise.

means that both shocks and contact discontinuities are tracked and resolved. While there is not a clear best scheme, the important aspect for us is that the FD-10-6-2-2 method maintains reasonable shock capturing ability and is not significantly more diffuse than FD-2.

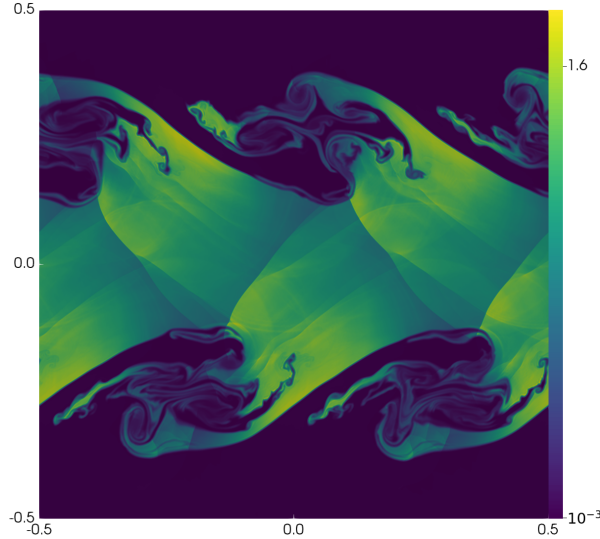


Figure 9. Rest mass density ρ from a high-resolution, 1408^2 , Kelvin-Helmholtz instability simulation at $t = 1.6$. The results in figure 10 below should be compared to this.

3.8. Orszag-Tang vortex

The relativistic version of the Orszag-Tang vortex is a 2-dimensional test case for GRMHD systems [67]. The initial conditions (and hence the states at later times) are periodic in both x and y with period 1. The initial conditions are:

$$\rho = \frac{25}{36\pi}, \quad (73)$$

$$p = \frac{5}{12\pi}, \quad (74)$$

$$v^i = \left[-\frac{1}{2} \sin(2\pi y), \frac{1}{2} \sin(2\pi x), 0 \right] \quad (75)$$

$$B^i = \left[-\frac{1}{\sqrt{4\pi}} \sin(2\pi y), \frac{1}{\sqrt{4\pi}} \sin(4\pi x), 0 \right] \quad (76)$$

closed by an ideal equation of state with $\Gamma = 5/3$. We use a domain $[0, 1]^3$ with periodic boundary conditions and evolve until a final time $t_f = 1$ using a CFL factor of 0.7.

We plot the rest mass density ρ at the final time $t_f = 1$ in figure 12 for simulations using the PPAO9-5-2-1 reconstruction scheme but using different order FD derivatives.

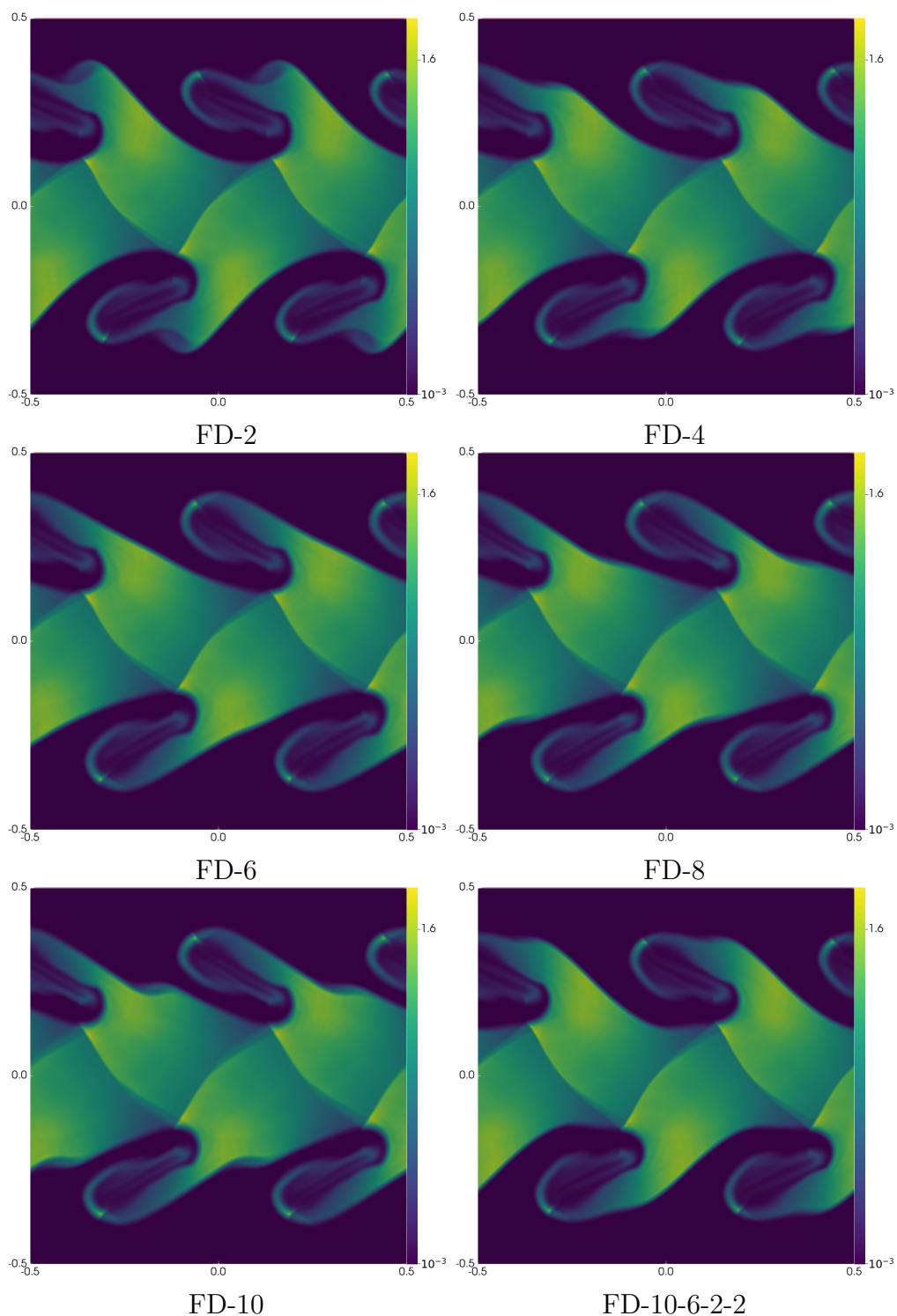


Figure 10. Kelvin-Helmholtz instability ρ at $t = 1.6$ showing the results using different FD derivative orders and always using the PPAO9-5-2-1 reconstruction method. In all cases the scheme is stable, though the FD-2 case is able to resolve additional small-scale vortices and the FD-10-6-2-2 case is almost able to resolve them. Reducing the CFL factor to 0.5 allows the FD-10-6-2-2 scheme to resolve the additional vortices.

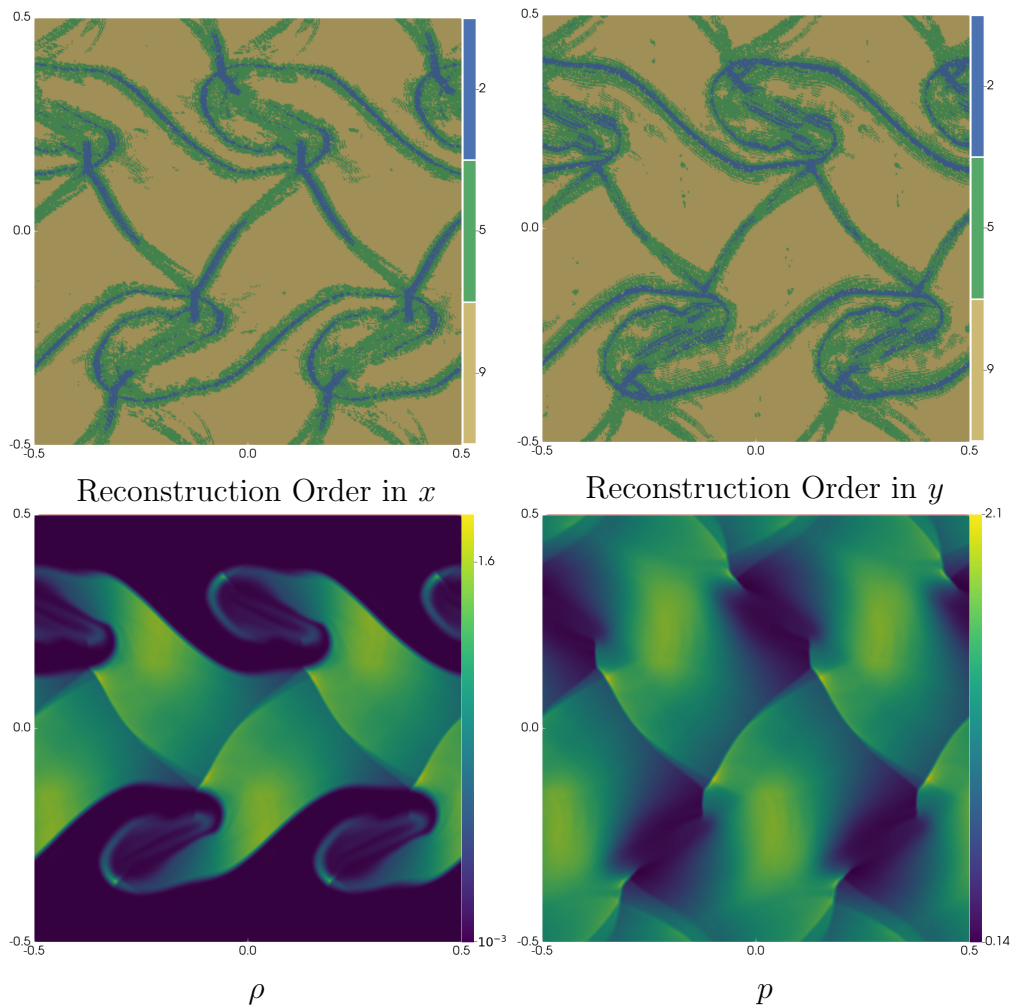


Figure 11. Results from the Kelvin-Helmholtz instability problem. The panels in the top row show the reconstruction and FD derivative order used in the x -direction (left) and y -direction (right) at the final time, while the bottom left panel shows the rest mass density and the bottom right the pressure at the final time. We see that the adaptive-order FD scheme accurately tracks non-smooth features in the solution, specifically the rest mass density and pressure, adjusting the order as necessary.

All schemes perform equally well with no discernible differences between them. We show the reconstruction order alongside ρ and pressure p in figure 13, nicely demonstrating that the PPAO scheme accurately tracks non-smooth features in both ρ and p for this problem as well.

3.9. Slab jet

To study our scheme's ability to handle explosions akin to what one would encounter in core-collapse supernova simulations, we run a slab jet simulation similar to that of [54]. We use the domain $[-0.5, 20] \times [-14, 14] \times [-0.5, 0.5]$ with resolution $176 \times 352 \times 11$.

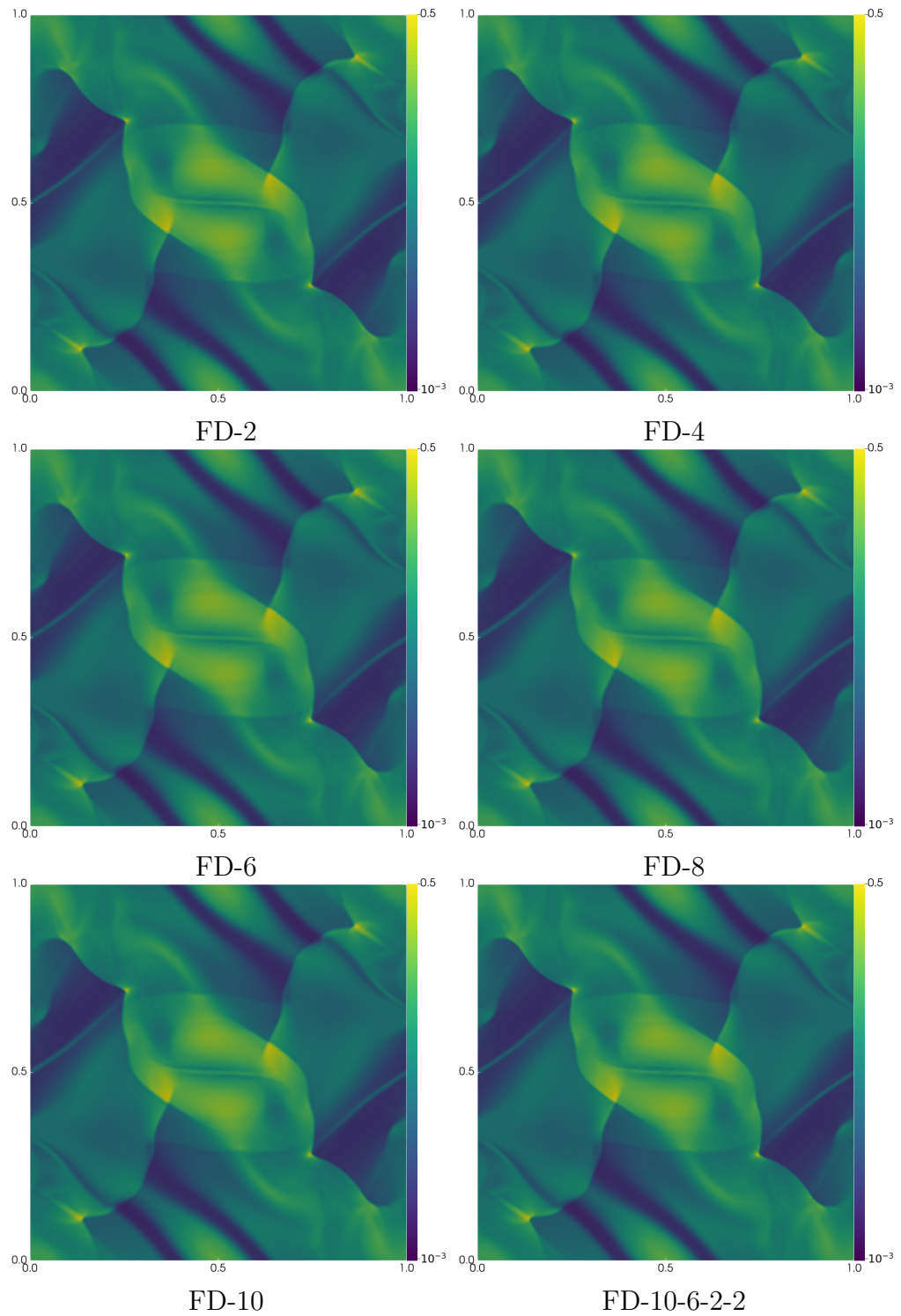


Figure 12. Orszag-Tang vortex ρ at $t = 1$ showing the results using different FD derivative orders and always using the PPAO9-5-2-1 reconstruction method. In all cases the scheme perform equally well for resolving the rest mass density.

We impose periodic boundary conditions in the z -direction and use Dirichlet boundary

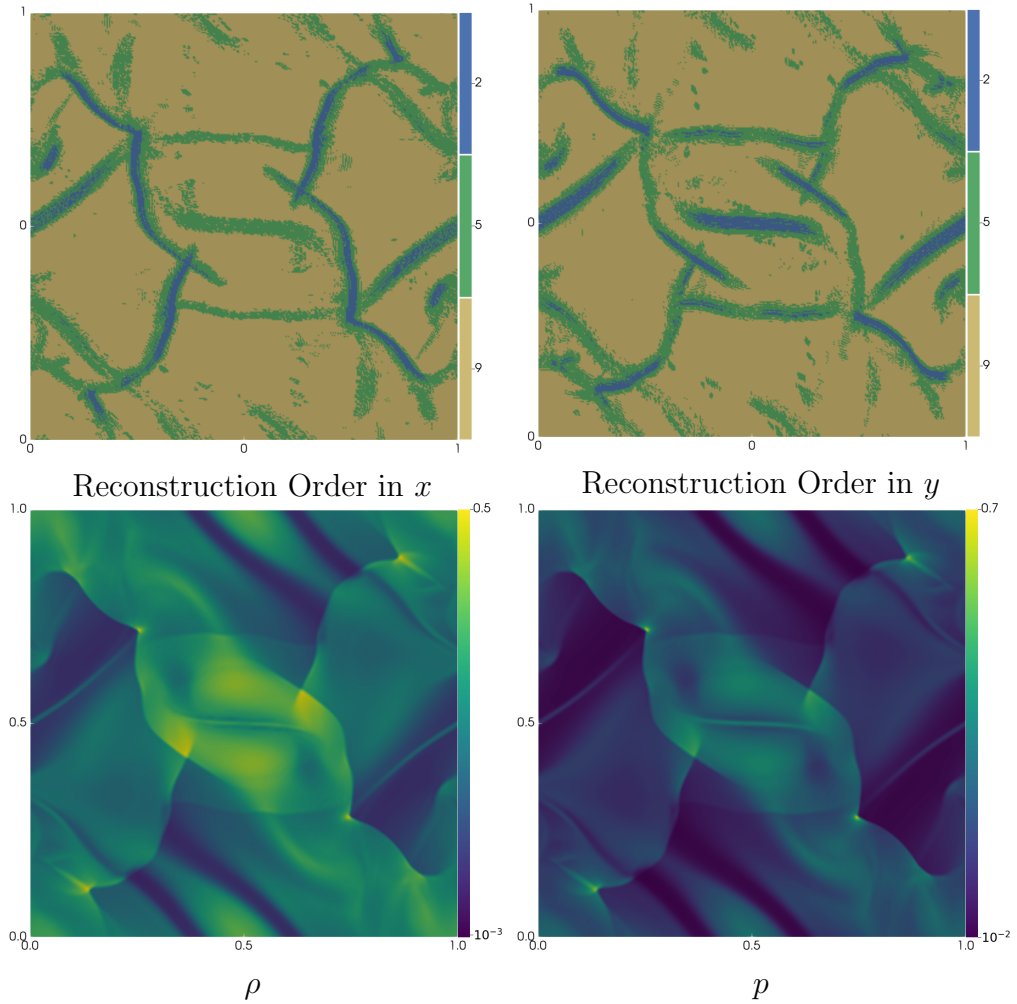


Figure 13. Results from the Orszag-Tang vortex. The panels in the top row show the reconstruction and FD derivative order used in the x -direction (left) and y -direction (right) at the final time, while the bottom left panel shows the rest mass density and the bottom right the pressure at the final time. We see that the adaptive-order FD scheme accurately tracks non-smooth features in the solution, specifically the rest mass density and pressure, adjusting the order as necessary.

conditions fixed to the initial conditions in x and y . The initial conditions are given by

$$\rho = \begin{cases} 10, & |y| < 0.5 \text{ and } x \leq 0 \\ 0.1, & \text{otherwise,} \end{cases} \quad (77)$$

$$p = 0.01, \quad (78)$$

$$u^i = \begin{cases} (20, 0, 0), & |y| < 0.5 \text{ and } x \leq 0 \\ (0, 0, 0), & \text{otherwise,} \end{cases} \quad (79)$$

$$B^i = (1, 0, 0), \quad (80)$$

and an ideal fluid equation of state is used with $\Gamma = 4/3$. We evolve to a final time of $t_f = 27$ with a CFL factor of 0.5. We find that for larger CFLs the FD-4, FD-6, FD-8,

and FD-10 algorithms become unstable.

We plot the rest mass density ρ at the final time $t_f = 27$ in figure 14 for simulations using the PPAO9-5-2-1 reconstruction scheme with various FD derivative orders. The FD-4 and FD-8 schemes produce significant deviations from symmetry about the $y = 0$ plane, while all other scheme preserve the symmetry quite well. In particular, we find that the FD derivative order adaptation (FD-10-6-2-2) is as robust as the FD-2 scheme, and can be run with larger CFL factors than the non-adaptive high-order derivatives.

3.10. TOV star

To test the proposed method's ability to simulate fluids in curved spacetimes, we evolve a Tolman-Oppenheimer-Volkoff (TOV) star [69, 70]. We perform simulations of both magnetized and non-magnetized TOV stars. We adopt the same configuration as in [71, 45, 32]. Specifically, we use a polytropic equation of state,

$$p(\rho) = K\rho^\Gamma \quad (81)$$

with $\Gamma = 2$, $K = 100$, and a central density $\rho_c = 1.28 \times 10^{-3} M_\odot^{-2}$. This choice of K and Γ mean we use geometric units where $G = c = M_\odot = 1$. For the magnetized case, we choose a magnetic field given by a vector potential

$$A_\phi = A_b (x^2 + y^2) \max(p - p_{\text{cut}}, 0)^{n_s}, \quad (82)$$

with $A_b = 2500$, $p_{\text{cut}} = 0.04 p_{\text{max}}$, and $n_s = 2$. This configuration yields a magnetic field strength in CGS units of $|B_{\text{CGS}}| = 1.03 \times 10^{16}$ G. The magnetic field is only a perturbation to the dynamics of the star, since $(p_{\text{mag}}/p)(r = 0) \sim 5 \times 10^{-5}$. The magnetic field is given by

$$B^x = -\frac{1}{\sqrt{\gamma}} \frac{xz}{r} A_b n_s (p - p_{\text{cut}})^{n_s-1} \partial_r p, \quad (83)$$

$$B^y = -\frac{1}{\sqrt{\gamma}} \frac{yz}{r} A_b n_s (p - p_{\text{cut}})^{n_s-1} \partial_r p, \quad (84)$$

$$B^z = \frac{A_b}{\sqrt{\gamma}} \left[2(p - p_{\text{cut}})^{n_s} + \frac{x^2 + y^2}{r} n_s (p - p_{\text{cut}})^{n_s-1} \partial_r p \right], \quad (85)$$

away from $r = 0$ and by

$$B^x = 0, \quad (86)$$

$$B^y = 0, \quad (87)$$

$$B^z = \frac{A_b}{\sqrt{\gamma}} 2(p - p_{\text{cut}})^{n_s}, \quad (88)$$

at $r = 0$.

All simulations are done in full 3d with no symmetry assumptions, but in the Cowling approximation, i.e. the spacetime is static. We use a cube $[-13, 13]^3$ in geometric units, which is slightly higher resolution than was used in [71, 45, 32]. We convert grid spacing to meters assuming a maximum mass of the neutron star of $M_{\max} = 2M_{\odot}$. We run simulations to a final time of $t_f = 5\text{ms}$ and monitor the maximum density over the domain as a function of time. In figure 15 we plot the relative change of the maximum rest mass density at three resolutions in the left panels and its power spectrum in the right panels. We compare the oscillation frequencies to the known frequencies [72, 73] and find good agreement in all cases. In particular, the PPAO9-5-2-2+FD-10-6-2-2 scheme very nicely resolves the seven frequencies plotted in figure 15. The PPAO5-2-2+FD-6-2-2 scheme starts to lose accuracy around the sixth peak, while PPAO5-2-2+FD-4 resolves the first six frequencies and arguably the seventh, but not as cleanly as the PPAO9-5-2-2+FD-10-6-2-2 scheme. Overall, our PPAO scheme works very well for TOV simulations. We do not plot the magnetized case since the behavior is effectively identical to the non-magnetized case, so much so that the plots are indistinguishable by eye. In figure 16 we show volume renderings of the $z = -0.1$ plane for the three different methods at the highest resolution. The PPAO5-2-2+FD-4 scheme smears the surface of the star out more than the two adaptive schemes, while PPAO9-5-2-2+FD-10-6-2-2 has spurious artifacts just outside the star. Given that these artifacts are absent in the PPAO5-2-2+FD-6-2-2 case, it might be possible to more aggressively drop from ninth to fifth order to remove them, but we have not tested this. Ultimately, this leads us to conclude that the adaptive scheme is able to produce crisp surfaces while achieving high order in smooth regions.

3.11. Rotating neutron star

As a final challenging 3d test case, we simulate a uniformly rotating neutron star with a ratio of polar to equatorial radii of 0.7, as in [45, 32] and similar to [74]. The initial data is constructed using the `RotNS` code described in [75, 76]. We again use a polytropic equation of state with $\Gamma = 2$ and $K = 100$. The simulations are done on a cubical domain of size $[-13, 13] \times [-13, 13] \times [-11, 11]$ to give roughly the same number of grid points across the star in all three dimensions. We show the ratio of the maximum rest mass density as a function of time to the maximum rest mass density at $t = 0$ in the left panels of figure 17, while the right panels show the power spectrum of the rest mass

density ratio. We show three different numerical schemes, PPAO5-2-2+FD-4, PPAO5-2-2+FD-6-2-2, and PPAO9-5-2-2+FD-10-6-2-2. We see that the adaptive-order derivative schemes are less dissipative while also resolving high-frequency radial pulsations. This demonstrates that our proposed adaptive-order schemes are able to produce stable long-term simulations of interesting astrophysical systems, and marks the first set of simulations that are ninth order in space.

4. Conclusions

We presented a new positivity-preserving adaptive-order (PPAO) finite-difference scheme that adjusts both the order of the unlimited cell-centered polynomial and the order of the finite-difference derivative based on a new oscillation indicator and physical admissibility criterion. The scheme reconstructs the primitive variables, which makes satisfying physical realizability relatively easy even for complicated systems such as general relativistic magnetohydrodynamics. The scheme does not make any assumptions about what the physical realizability conditions are and allows for combining an arbitrary number of admissibility conditions when selecting the reconstruction polynomial. We implemented the PPAO scheme in the publicly available code `SpECTRE` [49]. To demonstrate the efficacy of the proposed scheme, we perform a number of standard and difficult test problems in 1d, 2d, and 3d general relativistic magnetohydrodynamics. The scheme was also used to successfully simulate hybrid quark-hadron stars in [77]. The PPAO scheme is capable of evolving strongly magnetized and rotating neutron stars, and adapting the order of the FD derivative proves to significantly increase the robustness for challenging test problems. Adapting the FD derivative order also allows simulations to remain stable with larger time step sizes than when only high-order FD derivatives are used. Given the promising results, we share the viewpoint of [23] that physical realizability of the solution is as important as conservation.

We plan on adopting the flux limiter of [22, 13] to arrive at a scheme that is positivity-preserving for both the reconstruction and the time integration. Additionally, we have combined the PPAO scheme with our discontinuous Galerkin-finite difference hybrid scheme [32] and are working towards using the PPAO scheme to evolve the spacetime together with the GRMHD equations. We are also adding support for moving and semi-unstructured meshes, like cubed-sphere domains. The PPAO scheme naturally lends itself to semi-unstructured meshes since the linear polynomial can be obtained

from any grid structure with our admissibility criterion remaining easily implemented.

Acknowledgments

We are grateful to Michael Pajkos for feedback and informative discussions on the paper, especially the visualizations. SpECTRE uses Charm++/Converse [78, 79], which was developed by the Parallel Programming Laboratory in the Department of Computer Science at the University of Illinois at Urbana-Champaign. SpECTRE uses Blaze [80, 81], HDF5 [82], the GNU Scientific Library (GSL) [83], yaml-cpp [84], pybind11 [85], libsharp [86], and LIBXSMM [87]. The figures in this article were produced with matplotlib [88, 89], NumPy [90], and ParaView [91, 92]. Computations were performed with the Wheeler cluster at Caltech. This work was supported in part by the Sherman Fairchild Foundation and by NSF Grants PHY-2011961, PHY-2011968, and OAC-2209655 at Caltech, and NSF Grants PHY-2207342 and OAC-2209655 at Cornell. This work was supported in part by NSF grants PHY-1654359 and PHY-2208014, by the Dan Black Family Trust, and by Nicholas and Lee Begovich.

Appendix A. Use with discontinuous Galerkin-finite difference hybrid methods

We ultimately will use our PPAO scheme together with our discontinuous Galerkin-FD (DG-FD) hybrid method [32]. We leave a detailed discussion to future work, but briefly summarize our approach here. In practice we expect to use PPAO5-2-1 with derivative orders 4-2-2 (or possibly 6-2-2) to achieve formally fourth (fifth) order convergence on the FD grid, while the discontinuous Galerkin (DG) method will be at least sixth order. One question is whether to use the high-order flux G or the second-order flux $G^{(2)}$ on boundaries between DG and FD. Using $G^{(2)}$ significantly simplifies the code but formally violates conservation. However, if the DG solver is being used, the solution is smooth anyway, meaning that no discontinuities are nearby, and so strict conservation is not necessary. We advocate for using $G^{(2)}$ given the simplicity this offers. One way of guaranteeing the DG-FD interfaces are far from discontinuities is to use a halo of FD cells around discontinuities.

References

- [1] S. K. Godunov. A difference method for numerical calculation of discontinuous solutions of the equations of hydrodynamics. *Mat. Sb. (N.S.)*, 47(89):271–306, 1959.
- [2] S Chakravarthy, Ami Harten, and Stanley Osher. Essentially non-oscillatory shock-capturing schemes of arbitrarily-high accuracy. In *24th Aerospace Sciences Meeting*, page 339, 1986.
- [3] Ami Harten, Stanley Osher, Björn Engquist, and Sukumar R Chakravarthy. Some results on uniformly high-order accurate essentially nonoscillatory schemes. *Applied Numerical Mathematics*, 2(3-5):347–377, 1986.
- [4] Ami Harten, Bjorn Engquist, Stanley Osher, and Sukumar R Chakravarthy. Uniformly high order accurate essentially non-oscillatory schemes, III. *Journal of Computational Physics*, 71(2):231 – 303, 1987.
- [5] Chi-Wang Shu and Stanley Osher. Efficient implementation of essentially non-oscillatory shock-capturing schemes. *Journal of Computational Physics*, 77(2):439 – 471, 1988.
- [6] Chi-Wang Shu and Stanley Osher. Efficient implementation of essentially non-oscillatory shock-capturing schemes, II. *Journal of Computational Physics*, 83(1):32 – 78, 1989.
- [7] Guang-Shan Jiang and Chi-Wang Shu. Efficient implementation of weighted ENO schemes. *Journal of Computational Physics*, 126(1):202 – 228, 1996.
- [8] Xu-Dong Liu, Stanley Osher, and Tony Chan. Weighted essentially non-oscillatory schemes. *Journal of Computational Physics*, 115(1):200 – 212, 1994.
- [9] Xiaogang Deng and Hanxin Zhang. Developing high-order weighted compact nonlinear schemes. *Journal of Computational Physics*, 165(1):22 – 44, 2000.
- [10] *Computational Analysis of Characteristics and Mach Number Effects on Noise Emission From Ideally Expanded Highly Supersonic Free-Jet*, volume Volume 2: Fora, Parts A and B of *Fluids Engineering Division Summer Meeting*, 07 2007.
- [11] Shuhai Zhang, Shufen Jiang, and Chi-Wang Shu. Development of nonlinear weighted compact schemes with increasingly higher order accuracy. *Journal of Computational Physics*, 227(15):7294 – 7321, 2008.
- [12] David Radice, Luciano Rezzolla, and Filippo Galeazzi. Beyond second-order convergence in simulations of binary neutron stars in full general-relativity. *Mon. Not. Roy. Astron. Soc.*, 437:L46–L50, 2014.
- [13] David Radice, Luciano Rezzolla, and Filippo Galeazzi. High-Order Fully General-Relativistic Hydrodynamics: new Approaches and Tests. *Class. Quant. Grav.*, 31:075012, 2014.
- [14] Elias R. Most, L. Jens Papenfort, and Luciano Rezzolla. Beyond second-order convergence in simulations of magnetized binary neutron stars with realistic microphysics. *Mon. Not. Roy. Astron. Soc.*, 490(3):3588–3600, 2019.
- [15] Carolyn A. Raithel and Vasileios Paschalidis. Improving the convergence order of binary neutron star merger simulations in the Baumgarte- Shapiro-Shibata-Nakamura formulation. *Phys. Rev. D*, 106(2):023015, 2022.
- [16] Federico Cipolletta, Jay Vijay Kalinani, Edoardo Giangrandi, Bruno Giacomazzo, Riccardo Ciolfi, Lorenzo Sala, and Beatrice Giudici. Spritz: General Relativistic Magnetohydrodynamics with Neutrinos. *Class. Quant. Grav.*, 38(8):085021, 2021.

- [17] E. F. Toro. Riemann Solvers and Numerical Methods for Fluid Dynamics. Springer-Verlag Berlin Heidelberg, 2009.
- [18] Taku Nonomura and Kozo Fujii. Robust explicit formulation of weighted compact nonlinear scheme. Computers & Fluids, 85:8 – 18, 2013. International Workshop on Future of CFD and Aerospace Sciences.
- [19] Lucie Freret, Lucian Ivan, Hans De Sterck, and Clinton P. Groth. A high-order finite-volume method with anisotropic AMR for ideal MHD flows. AIAA, 2017-0845, January 2017.
- [20] Olindo Zanotti and Michael Dumbser. Efficient conservative ADER schemes based on WENO reconstruction and space-time predictor in primitive variables. Computational Astrophysics and Cosmology, 3:1, January 2016.
- [21] Lucian Ivan and Clinton P.T. Groth. High-order solution-adaptive central essentially non-oscillatory (CENO) method for viscous flows. Journal of Computational Physics, 257:830–862, 2014.
- [22] Xiangyu Y. Hu, Nikolaus A. Adams, and Chi-Wang Shu. Positivity-preserving method for high-order conservative schemes solving compressible Euler equations. Journal of Computational Physics, 242:169 – 180, 2013.
- [23] Dinshaw S. Balsara. Self-adjusting, positivity preserving high order schemes for hydrodynamics and magnetohydrodynamics. Journal of Computational Physics, 231(22):7504 – 7517, 2012.
- [24] Dinshaw S. Balsara, Sudip Garain, and Chi-Wang Shu. An efficient class of WENO schemes with adaptive order. Journal of Computational Physics, 326:780 – 804, 2016.
- [25] Di Sun, Feng Qu, and Chao Yan. An efficient adaptive high-order scheme based on the weno process. Computers & Fluids, 140:81 – 96, 2016.
- [26] Matteo Semplice and Giuseppe Visconti. Efficient implementation of adaptive order reconstructions. Journal of Scientific Computing, 83(1):1–27, 2020.
- [27] Federico Guercilena, David Radice, and Luciano Rezzolla. Entropy-limited hydrodynamics: a novel approach to relativistic hydrodynamics. Comput. Astrophys. Cosmol., 4:3, 2017.
- [28] Georgios Doulis, Florian Atteneder, Sebastiano Bernuzzi, and Bernd Brügmann. Entropy-limited higher-order central scheme for neutron star merger simulations. Phys. Rev. D, 106(2):024001, 2022.
- [29] S. Clain, S. Diot, and R. Loubère. A high-order finite volume method for systems of conservation laws—multi-dimensional optimal order detection (MOOD). Journal of Computational Physics, 230(10):4028 – 4050, 2011.
- [30] S. Diot, S. Clain, and R. Loubère. Improved detection criteria for the multi-dimensional optimal order detection (MOOD) on unstructured meshes with very high-order polynomials. Computers & Fluids, 64:43 – 63, 2012.
- [31] S. Diot, R. Loubère, and S. Clain. The multidimensional optimal order detection method in the three-dimensional case: very high-order finite volume method for hyperbolic systems. International Journal for Numerical Methods in Fluids, 73(4):362–392, 2013.
- [32] Nils Deppe, François Hébert, Lawrence E. Kidder, and Saul A. Teukolsky. A high-order shock capturing discontinuous Galerkin–finite difference hybrid method for GRMHD. Class. Quant. Grav., 39(19):195001, 2022.
- [33] A. Suresh and H.T. Huynh. Accurate monotonicity-preserving schemes with Runge–Kutta time

- stepping. Journal of Computational Physics, 136(1):83–99, 1997.
- [34] Per-Olof Persson and Jaime Peraire. Sub-cell shock capturing for discontinuous Galerkin methods. In 44th AIAA Aerospace Sciences Meeting and Exhibit, pages 1–13. American Institute of Aeronautics and Astronautics, Inc., 2006.
- [35] David Gottlieb and Steven A. Orszag. Numerical Analysis of Spectral Methods. Society for Industrial and Applied Mathematics, 1977.
- [36] Bram Van Leer. Towards the ultimate conservative difference scheme. IV. a new approach to numerical convection. Journal of Computational Physics, 23(3):276–299, 1977.
- [37] Xiangxiong Zhang and Chi-Wang Shu. Maximum-principle-satisfying and positivity-preserving high-order schemes for conservation laws: survey and new developments. Proceedings of the Royal Society A: Mathematical, Physical and Engineering Sciences, 467(2134):2752–2776, 2011.
- [38] Xiangxiong Zhang and Chi-Wang Shu. On positivity-preserving high order discontinuous Galerkin schemes for compressible Euler equations on rectangular meshes. Journal of Computational Physics, 229(23):8918 – 8934, 2010.
- [39] Xiangxiong Zhang and Chi-Wang Shu. Positivity-preserving high order finite difference WENO schemes for compressible Euler equations. Journal of Computational Physics, 231(5):2245 – 2258, 2012.
- [40] Andrew J. Christlieb, Yuan Liu, Qi Tang, and Zhengfu Xu. Positivity-Preserving Finite Difference Weighted ENO Schemes with Constrained Transport for Ideal Magnetohydrodynamic Equations. SIAM Journal on Scientific Computing, 37(4):A1825–A1845, January 2015.
- [41] Kailiang Wu and Chi-Wang Shu. A Provably Positive Discontinuous Galerkin Method for Multidimensional Ideal Magnetohydrodynamics. SIAM Journal on Scientific Computing, 40(5):B1302–B1329, January 2018.
- [42] L. Del Zanna, O. Zanotti, N. Bucciantini, and P. Londrillo. ECHO: an Eulerian Conservative High Order scheme for general relativistic magnetohydrodynamics and magnetodynamics. Astron. Astrophys., 473:11–30, 2007.
- [43] Yuxi Chen, Gábor Tóth, and Tamas I. Gombosi. A fifth-order finite difference scheme for hyperbolic equations on block-adaptive curvilinear grids. Journal of Computational Physics, 305:604–621, 2016.
- [44] Amiram Harten, Peter D. Lax, and Bram van. Leer. On upstream differencing and Godunov-type schemes for hyperbolic conservation laws. SIAM Review, 25(1):35–61, 1983.
- [45] Nils Deppe et al. Simulating magnetized neutron stars with discontinuous Galerkin methods. Phys. Rev. D, 105(12):123031, 2022.
- [46] Luis Antón, Olindo Zanotti, Juan A. Miralles, José M. Martí, José M. Ibáñez, José A. Font, and José A. Pons. Numerical 3+1 general relativistic magnetohydrodynamics: a local characteristic approach. The Astrophysical Journal, 637:296–312, January 2006.
- [47] Jose A. Font. Numerical hydrodynamics and magnetohydrodynamics in general relativity. Living Rev. Rel., 11:7, 2008.
- [48] Thomas W. Baumgarte and Stuart L. Shapiro. Numerical Relativity: Solving Einstein’s Equations on the Computer. Cambridge University Press, 2010.
- [49] Nils Deppe, William Throwe, Lawrence E. Kidder, Nils L. Vu, François Hébert, Jordan Moxon,

- Cristóbal Armaza, Marceline S. Bonilla, Yoonsoo Kim, Prayush Kumar, Geoffrey Lovelace, Alexandra Macedo, Kyle C. Nelli, Eamonn O’Shea, Harald P. Pfeiffer, Mark A. Scheel, Saul A. Teukolsky, Nikolas A. Wittek, et al. *SpECTRE v2023.04.07*. 10.5281/zenodo.7809262, 4 2023.
- [50] J.R. Dormand and P.J. Prince. Runge-Kutta triples. *Computers & Mathematics with Applications*, 12(9, Part A):1007–1017, 1986.
- [51] Ernst Hairer, Syvert Norsett, and Gerhard Wanner. *Solving Ordinary Differential Equations I: Nonstiff Problems*, volume 8. Springer, 01 1993.
- [52] William H. Press, Saul A. Teukolsky, William T. Vetterling, and Brian P. Flannery. *Numerical Recipes 3rd Edition: The Art of Scientific Computing*. Cambridge University Press, sep 2007.
- [53] Dinshaw Balsara. Total variation diminishing scheme for relativistic magnetohydrodynamics. *The Astrophysical Journal Supplement Series*, 132(1):83–101, January 2001.
- [54] S. S. Komissarov. A Godunov-type scheme for relativistic magnetohydrodynamics. *Monthly Notices of the Royal Astronomical Society*, 303(2):343–366, 1999.
- [55] T. Leismann, L. Antón, M. A. Aloy, E. Müller, J. M. Martí, J. A. Miralles, and J. M. Ibáñez. Relativistic MHD simulations of extragalactic jets. *Astron. Astrophys.*, 436:503–526, June 2005.
- [56] Francesco Fambri, Michael Dumbser, Sven Köppel, Luciano Rezzolla, and Olindo Zanotti. ADER discontinuous Galerkin schemes for general-relativistic ideal magnetohydrodynamics. *Mon. Not. Roy. Astron. Soc.*, 477(4):4543–4564, 2018.
- [57] Ami Harten. On a class of high resolution total-variation-stable finite-difference schemes. *SIAM Journal on Numerical Analysis*, 21(1):1–23, 1984.
- [58] Dinshaw S. Balsara and Daniel S. Spicer. A staggered mesh algorithm using high order Godunov fluxes to ensure solenoidal magnetic fields in magnetohydrodynamic simulations. *Journal of Computational Physics*, 149(2):270–292, March 1999.
- [59] Gábor Tóth. The $\nabla \cdot \mathbf{B} = 0$ constraint in shock-capturing magnetohydrodynamics codes. *Journal of Computational Physics*, 161(2):605–652, July 2000.
- [60] Zachariah B. Etienne, Yuk Tung Liu, and Stuart L. Shapiro. Relativistic magnetohydrodynamics in dynamical spacetimes: A new adaptive mesh refinement implementation. *Phys. Rev. D*, 82(8):084031, October 2010.
- [61] L. Del Zanna, N. Bucciantini, and P. Londrillo. An efficient shock-capturing central-type scheme for multidimensional relativistic flows. II. Magnetohydrodynamics. *Astron. Astrophys.*, 400:397–413, March 2003.
- [62] C. Richard DeVore. Flux-corrected transport techniques for multidimensional compressible magnetohydrodynamics. *Journal of Computational Physics*, 92(1):142–160, January 1991.
- [63] Philipp Mösta, Bruno C. Mundim, Joshua A. Faber, Roland Haas, Scott C. Noble, Tanja Bode, Frank Löffler, Christian D. Ott, Christian Reisswig, and Erik Schnetter. GRHydro: A new open source general-relativistic magnetohydrodynamics code for the Einstein Toolkit. *Class. Quant. Grav.*, 31:015005, 2014.
- [64] Kris Beckwith and James M. Stone. A second-order Godunov method for multi-dimensional relativistic magnetohydrodynamics. *Astrophysical Journal, Supplement*, 193(1):6, March 2011.
- [65] Thomas A. Gardiner and James M. Stone. An unsplit Godunov method for ideal MHD via constrained transport. *Journal of Computational Physics*, 205(2):509–539, May 2005.

- [66] James M. Stone, Thomas A. Gardiner, Peter Teuben, John F. Hawley, and Jacob B. Simon. Athena: A New Code for Astrophysical MHD. *Astrophysical Journal, Supplement*, 178(1):137–177, September 2008.
- [67] Kris Beckwith and James M. Stone. A second order Godunov method for multidimensional relativistic magnetohydrodynamics. *Astrophys. J. Suppl.*, 193:6, 2011.
- [68] Kevin Schaal, Andreas Bauer, Praveen Chandrashekar, Rüdiger Pakmor, Christian Klingenberg, and Volker Springel. Astrophysical hydrodynamics with a high-order discontinuous Galerkin scheme and adaptive mesh refinement. *Mon. Not. Roy. Astron. Soc.*, 453(4):4278–4300, 2015.
- [69] Richard C. Tolman. Static solutions of Einstein’s field equations for spheres of fluid. *Phys. Rev.*, 55:364–373, 1939.
- [70] J. R. Oppenheimer and G. M. Volkoff. On massive neutron cores. *Phys. Rev.*, 55:374–381, 1939.
- [71] Federico Cipolletta, Jay Vijay Kalinani, Bruno Giacomazzo, and Riccardo Ciolfi. Spritz: a new fully general-relativistic magnetohydrodynamic code. *Class. Quant. Grav.*, 37(13):135010, 2020.
- [72] Jose A. Font, Nikolaos Stergioulas, and Kostas D. Kokkotas. Nonlinear hydrodynamical evolution of rotating relativistic stars: Numerical methods and code tests. *Mon. Not. Roy. Astron. Soc.*, 313:678, 2000.
- [73] Nikolas Stergioulas, Jose A. Font, and Kostas D. Kokkotas. Nonlinear evolution of rotating relativistic stars. *Nucl. Phys. B Proc. Suppl.*, 80:0724, 2000.
- [74] José A. Font, Tom Goodale, Sai Iyer, Mark Miller, Luciano Rezzolla, Edward Seidel, Nikolaos Stergioulas, Wai-Mo Suen, and Malcolm Tobias. Three-dimensional numerical general relativistic hydrodynamics. II. Long-term dynamics of single relativistic stars. *Phys. Rev. D*, 65(8):084024, April 2002.
- [75] Gregory B. Cook, Stuart L. Shapiro, and Saul A. Teukolsky. Spin-up of a rapidly rotating star by angular momentum loss: Effects of general relativity. *The Astrophysical Journal*, 398:203, October 1992.
- [76] Gregory B. Cook, Stuart L. Shapiro, and Saul A. Teukolsky. Rapidly rotating neutron stars in general relativity: Realistic equations of state. *The Astrophysical Journal*, 424:823, April 1994.
- [77] Isaac Legred, Yoonsoo Kim, Nils Deppe, Katerina Chatziioannou, Francois Foucart, François Hébert, and Lawrence E. Kidder. Simulating neutron stars with a flexible enthalpy-based equation of state parametrization in SpECTRE. *Phys. Rev. D*, 107(12):123017, June 2023.
- [78] Laxmikant Kale et al. UIUC-PPL/charm: Charm++ version 7.0.0, October 2021.
- [79] Laxmikant V Kale and Sanjeev Krishnan. Charm++: Parallel programming with message-driven objects. In Gregory V. Wilson and Paul Lu, editors, *Parallel programming using C++*, pages 175–213. The MIT Press, 1996.
- [80] Klaus Iglberger, Georg Hager, Jan Treibig, and Ulrich Rüde. High performance smart expression template math libraries. In *2012 International Conference on High Performance Computing & Simulation (HPCS)*, pages 367–373, 2012.
- [81] Klaus Iglberger, Georg Hager, Jan Treibig, and Ulrich Rüde. Expression templates revisited: A performance analysis of current methodologies. *SIAM Journal on Scientific Computing*, 34(2):C42–C69, 2012.
- [82] The HDF Group. Hierarchical Data Format, version 5, 1997-2023.

<https://www.hdfgroup.org/HDF5/>.

- [83] M. Galassi et al. GNU Scientific Library Reference Manual. Network Theory Ltd., 3 edition, 2009.
- [84] Jesse Beder, Matthew Woehlke, Jens Breitbart, Scott Wolchok, Azamat H. Hackimov, Jamie Snape, Oliver Hamlet, Paul Novotny, Raul Tambre, Stefan Reinhold, Alain Vaucher, Alexander Zaitsev, Alexander Anokhin, Alexander Karatarakis, Andy Maloney, Antony Polukhin, Craig M. Brandenburg, Dan Ibanez, Denis Gladkikh, Florian Eich, Guillaume Dumont, Haydn Trigg, Jim King, Joel Frederico, Jonathan Hamilton, Joseph Langley, Lassi Hämäläinen, Matt Blair, Michael Welsh Duggan, Olli Wang, Patrick Stotko, Peter Levine, Petr Bena, Rodrigo Hernandez Cordoba, Ryan Schmidt, Simon Gene Gottlieb, Franz Prilmeier, Tanki Zhang, Tatsuyuki Ishi, Ted Lyngmo, Victor Mataré, Michael Konečný, and USDOE. `yaml-cpp`, 9 2009.
- [85] Wenzel Jakob, Jason Rhinelander, and Dean Moldovan. `pybind11` – seamless operability between `c++11` and `python`, 2017. <https://github.com/pybind/pybind11>.
- [86] M. Reinecke and D. S. Seljebotn. `Libsharp` - spherical harmonic transforms revisited. *Astron. Astrophys.*, 554:A112, June 2013.
- [87] Alexander Heinecke, Greg Henry, Maxwell Hutchinson, and Hans Pabst. `LIBXSMM`: Accelerating small matrix multiplications by runtime code generation. In Proceedings of the International Conference for High Performance Computing, Networking, Storage and Analysis, SC '16, pages 1–11. IEEE Press, 2016.
- [88] J. D. Hunter. `Matplotlib`: A 2d graphics environment. *Computing in Science & Engineering*, 9(3):90–95, 2007.
- [89] Thomas A Caswell, Michael Droettboom, Antony Lee, John Hunter, Eric Firing, Elliott Sales de Andrade, Tim Hoffmann, David Stansby, Jody Klymak, Nelle Varoquaux, Jens Hedegaard Nielsen, Benjamin Root, Ryan May, Phil Elson, Darren Dale, Jae-Joon Lee, Jouni K. Seppänen, Damon McDougall, Andrew Straw, Paul Hobson, Christoph Gohlke, Tony S Yu, Eric Ma, Adrien F. Vincent, Steven Silvester, Charlie Moad, Nikita Kniazev, hannah, Elan Ernest, and Paul Ivanov. `matplotlib/matplotlib`: REL: v3.3.0, July 2020.
- [90] Charles R. Harris, K. Jarrod Millman, Stéfan J. van der Walt, Ralf Gommers, Pauli Virtanen, David Cournapeau, Eric Wieser, Julian Taylor, Sebastian Berg, Nathaniel J. Smith, Robert Kern, Matti Picus, Stephan Hoyer, Marten H. van Kerkwijk, Matthew Brett, Allan Haldane, Jaime Fernández del Río, Mark Wiebe, Pearu Peterson, Pierre Gérard-Marchant, Kevin Sheppard, Tyler Reddy, Warren Weckesser, Hameer Abbasi, Christoph Gohlke, and Travis E. Oliphant. Array programming with `NumPy`. *Nature*, 585(7825):357–362, September 2020.
- [91] Utkarsh Ayachit. The ParaView Guide: A Parallel Visualization Application. Kitware, Inc., Clifton Park, NY, USA, 2015.
- [92] J. Ahrens, Berk Geveci, and C. Law. ParaView: An end-user tool for large-data visualization. Elsevier, 2005.

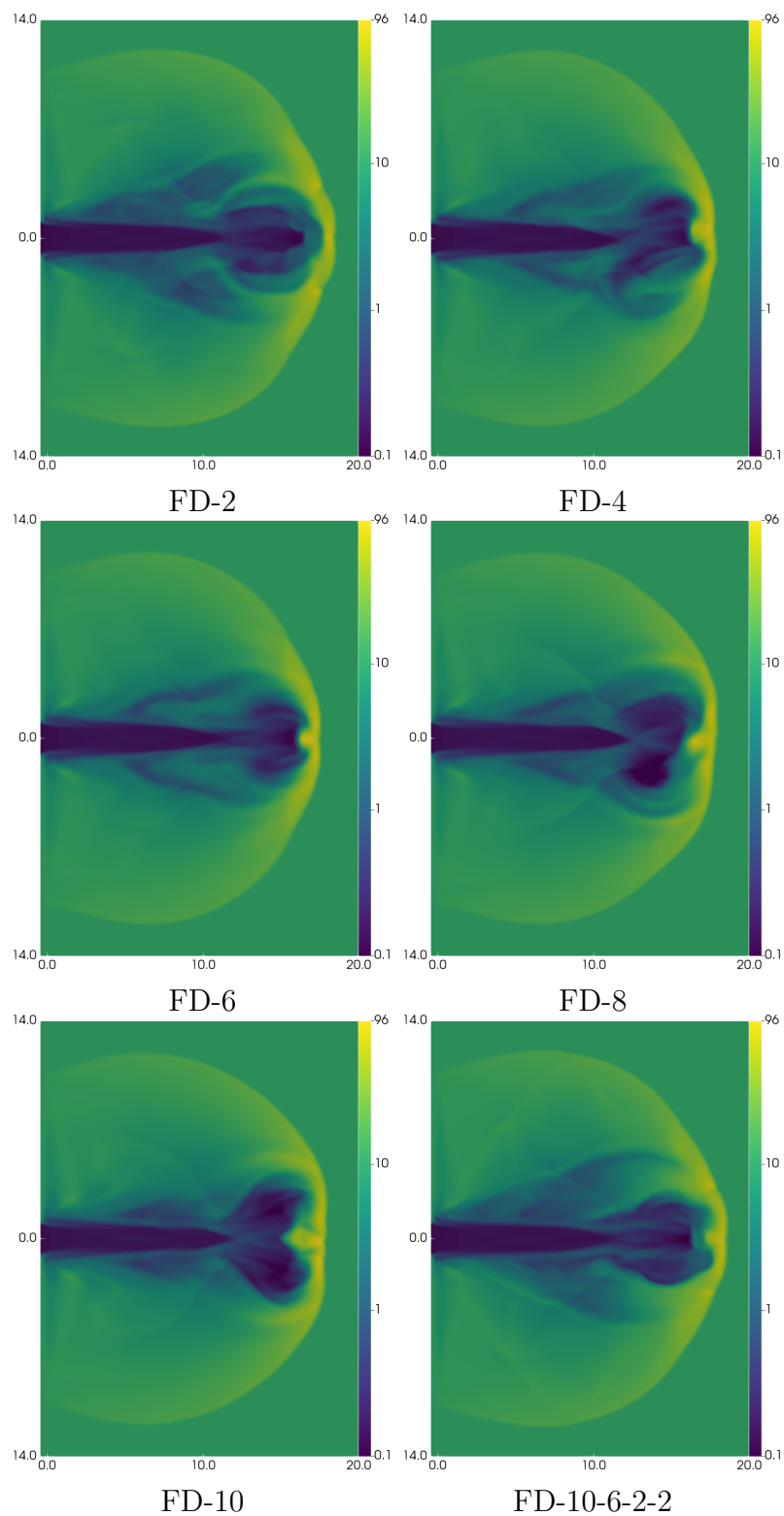


Figure 14. Slab jet simulation ρ at $t = 27$ showing the results using different FD derivative orders and always using the PPAO9-5-2-1 reconstruction method. We see significant symmetry breaking with FD-4 and FD-8, while all other schemes respect the symmetry quite well. Importantly, the FD-10-6-2-2 scheme is as robust as the FD-2 scheme while being very accurate.

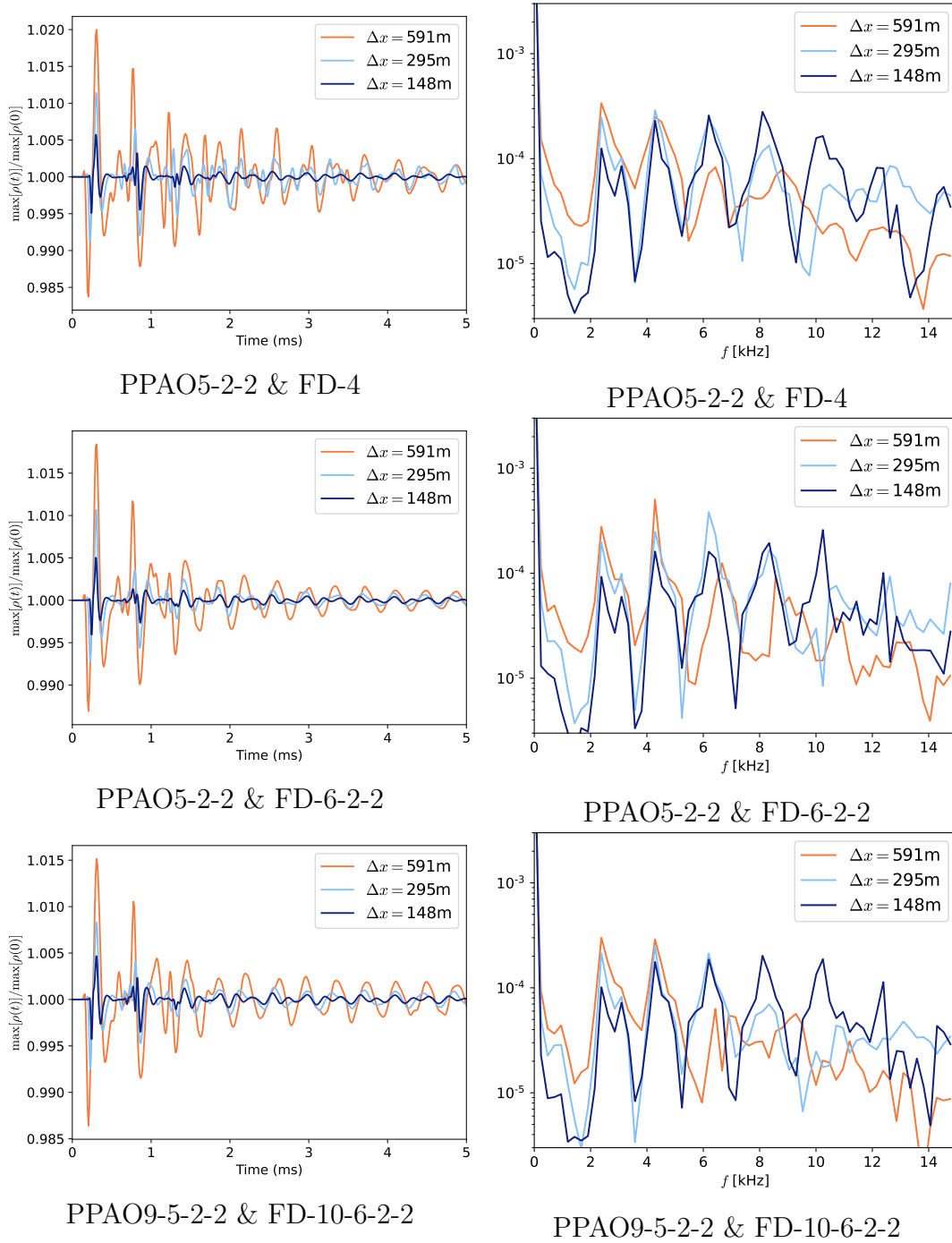


Figure 15. Results from evolutions of a TOV star to a final time of 5ms using different PPAO reconstruction and FD order schemes. The left panels show the maximum rest mass density as a function of time divided by the maximum rest mass density at $t = 0$, which oscillates about 1 with the amplitude decaying over time. The right panels show a power spectrum of the left panels with vertical dashed grey lines showing the analytically known radial oscillation frequencies [72, 73]. We see that the PPAO9-5-2-2 scheme does especially well at resolving higher frequency modes.

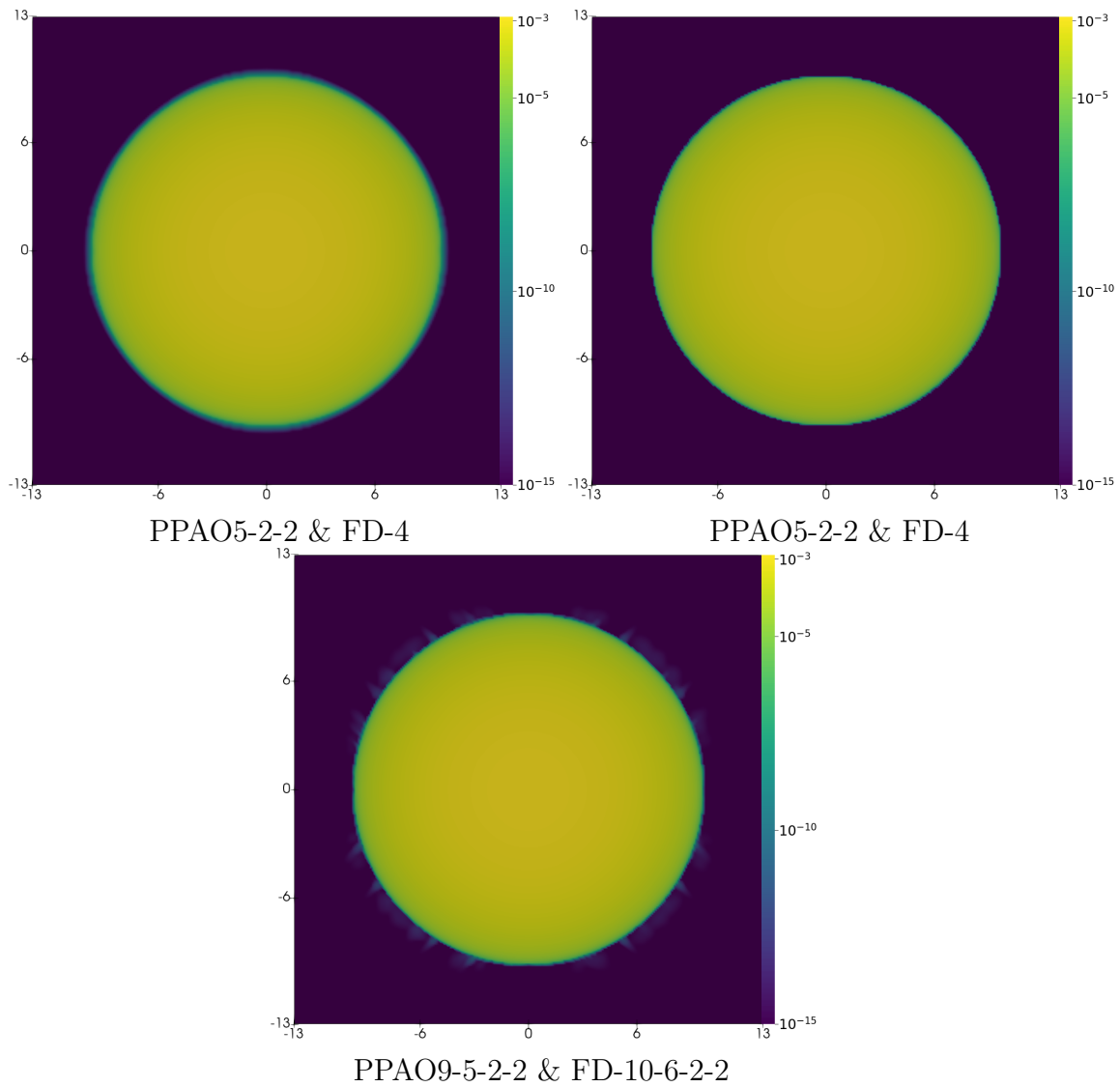


Figure 16. Visualization of the log of the rest mass density on the $z = -0.1$ plane at $t = 4.7\text{ms}$. The PPAO5-2-2+FD-4 scheme smears the surface more than the PPAO5-2-2+FD-6-2-2 scheme, while the PPAO9-5-2-2+FD-10-6-2-2 scheme produces spurious artifacts just outside the star. Dropping from ninth to fifth order earlier might remove the spurious artifacts, but we have not tested this. Ultimately, the adaptive order scheme is able to produce crisp surfaces while achieving high order in smooth regions.

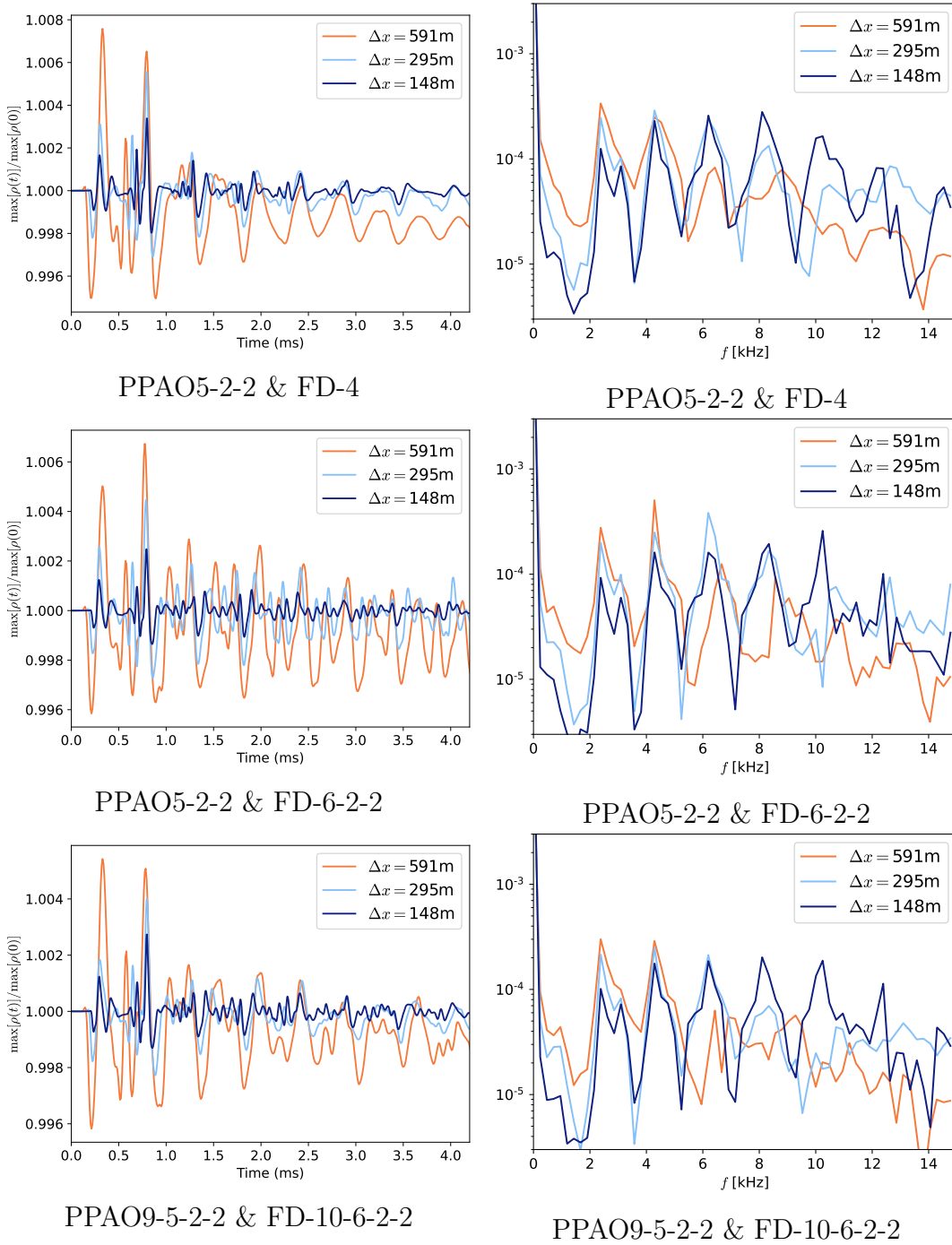


Figure 17. Results from evolutions of a rotating star with polar to equatorial radii ratio of 0.7 to a final time of 4.2ms using different PPAO reconstruction and FD order schemes. The left panels show the maximum rest mass density as a function of time divided by the maximum rest mass density at $t = 0$, which oscillates about 1 with the amplitude decaying over time. The right panels show a power spectrum of the left panels.